



HAL
open science

Crystallisation and fast cooling of the (meta)gabbro from the Chenaillet ophiolite (Western Alps): in-situ U-Pb dating of zircon, titanite, monazite and xenotime in textural context

Christian Nicollet, Jean-Louis Paquette, Emilie Bruand, Valérie Bosse, Inês Pereira

► To cite this version:

Christian Nicollet, Jean-Louis Paquette, Emilie Bruand, Valérie Bosse, Inês Pereira. Crystallisation and fast cooling of the (meta)gabbro from the Chenaillet ophiolite (Western Alps): in-situ U-Pb dating of zircon, titanite, monazite and xenotime in textural context. *Lithos*, 2022, 414-415, pp.106620. 10.1016/j.lithos.2022.106620 . insu-03852372

HAL Id: insu-03852372

<https://insu.hal.science/insu-03852372>

Submitted on 15 Nov 2022

HAL is a multi-disciplinary open access archive for the deposit and dissemination of scientific research documents, whether they are published or not. The documents may come from teaching and research institutions in France or abroad, or from public or private research centers.

L'archive ouverte pluridisciplinaire **HAL**, est destinée au dépôt et à la diffusion de documents scientifiques de niveau recherche, publiés ou non, émanant des établissements d'enseignement et de recherche français ou étrangers, des laboratoires publics ou privés.



Distributed under a Creative Commons Attribution - NonCommercial - NoDerivatives 4.0 International License

1 **Crystallisation and fast cooling of the (meta)gabbro from the Chenaillet**
2 **ophiolite (Western Alps): in-situ U-Pb dating of zircon, titanite, monazite and**
3 **xenotime in textural context.**

4 Christian Nicollet ¹, Jean-Louis Paquette ¹, Emilie Bruand ¹, Valérie Bosse ¹, Inês Pereira ¹

5 ¹Laboratoire Magmas et Volcans, Université Clermont Auvergne, CNRS, IRD, OPGC, F-63000 Clermont-Ferrand,
6 France

7 Keywords : Alps, Chenaillet ophiolite, metagabbro, fast cooling, LA-ICPMS in situ dating, accessory
8 minerals.

9 **Abstract**

10 The Chenaillet ophiolite, South of Montgenèvre (France), represents a preserved portion of
11 the alpine ocean. The gabbros form lenticular bodies 50 to 200 m thick and a few hundreds of meters
12 wide. They are intrusive in the serpentinites and often overlain by pillow-lavas. Plagiogranite/albitite
13 veins are rare and volumetrically negligible. The petrology of the gabbro s.s. show great details of the
14 progressive cooling of the massif, clinopyroxene are often rimmed by brown to green amphibole +/-
15 ilmenite/titanite. Thermometry on these amphibole assemblages indicates a retrograde temperature
16 evolution from late magmatic to subsolidus, between 950-900°C, 800-750°C, 600-500°C. In a shear
17 zone, a string of titanite associated with monazite and xenotime +/- ilmenite is located in a millimetric
18 greenschist layer whose temperature is estimated at 600-550°C. Accessories chemistry in this sample
19 allowed in situ dating by LA-ICPMS on thin section in textural context. In the same sample, we
20 performed U-Pb zircon dating, constraining the magmatic age, as well as U-Pb monazite, xenotime
21 and titanite dating for the metamorphic evolution. In a Tera-Wasserburg diagram, monazite, xenotime
22 and titanite yield 161.3 +/- 4.0 Ma, 161.5 +/- 2.4 Ma and 158.4 +/- 2.3 Ma lower intercept ages,

23 respectively, while the zircon from the same sample indicates an age of 161.0 +/- 0.8 Ma. Finally,
24 zircon dated in an albitite vein also yields a 161.8 ± 1.7 Ma age. These similar ages within the
25 analytical uncertainties show that magmatism and metamorphism were concomitant. Thermal
26 modelling predicts that a 150m thick gabbroic massif crystallizes in a few hundred years and cools
27 down in several thousand years. This is consistent with the ages reported in our study showing that
28 the retrograde metamorphism in this massif records fast cooling. The development of this retrograde
29 metamorphism required multiple fluid infiltrations during cooling. In the studied samples, 4 types of
30 titanites could be distinguished based on their chemistries. 3 types variously depleted in REE are
31 interpreted as related to water-driven fluids while another type has up to 10% REE, Y and Nb and
32 suggest a possible felsic source. The two potential sources of water promoting this fast cooling are
33 sea water-derived fluids and magmatic fluids exsolved from felsic veins.

34 **Introduction**

35 The Chenaillet ophiolite, South of Montgenève, in the Western Alps is one of the very well-
36 preserved portions of the alpine ophiolites, which represent remnants of the Tethys oceanic domain
37 (Figure 1). The alpine Tethys developed as a rather narrow basin, with a maximum width of less than
38 800 km and a very low spreading rate. It formed during a short-lived phase of magmatism between
39 165 Ma and 155 Ma (Manatschal and Muntener, 2009; McCarthy et al., 2021; Tribuzio et al 2016).
40 Alpine ophiolites constitute a heterogeneous lithosphere similar to that formed at slow/ultra-slow
41 spreading ridges or ocean-continent transition. They are mainly composed of variably serpentinised
42 mantle peridotites and irregularly distributed magmatic rocks composed of gabbroic lenses and dis-
43 continuous basaltic cover. Gabbros, troctolite, diorite and albitite are commonly found in alpine ophi-
44 olites and are thought to be the result of fractional crystallization of evolving melts and/or the inter-
45 action between a fractionating crystal mush with an external evolved melt (Rampone and Sanfilippo,
46 2021). Basaltic dykes are rare and the sheeted dyke complex associated with classical Penrose-type
47 model of ophiolites is lacking. Overall, these magmatic rocks have a geochemical affinity of MORB,

48 similar to that of oceanic basalts and kilometre-scale detachment faults accommodated the exhuma-
49 tion of mantle rocks and gabbros to the sea floor. Some of these ophiolites are formed in the mantle
50 of the continental margin and represent ocean-continent transition (OCT) while others constitute in-
51 tra-oceanic domains (Manatschal and Muntener, 2009).

52 According to these authors, the Chenaillet ophiolite would represent an intra-oceanic domain.
53 The massif of the Mont Chenaillet has overlapped the continental crust and displays only weak effects
54 of alpine deformation and metamorphism related to the alpine collision at 33 Ma. This ophiolite is
55 characterized by the occurrence of exhumed serpentinitised mantle, intruded by small lenses of gabbros;
56 a voluminous volcanic complex is fed by rare dykes (Mével et al., 1978; Bertrand et al., 1982, 1987;
57 Caby, 1995; Chalot-Prat, 2005; Manatschal et al, 2011 and reference therein). In the Chenaillet massif,
58 various rock types such as gabbros, troctolite, diorite and albitite, have been dated (Costa and Caby,
59 2001; Chalot-Prat, 2005; Desmurs et al., 2002, for a review see Li et al., 2013). These latter suggested
60 that the troctolites and albitites crystallized synchronously at about 165 Ma, which is consistent with
61 age estimates of the mantle exhumation of the Alpine Tethys ocean after continental breakup
62 (Manastchal and Muntener, 2009). This date is also consistent with the middle-bathonian age of the
63 oceanic sediments of the neighbouring Lago Nero-Replatte unit which is considered to be the base of
64 the sedimentary succession associated with the ophiolite body (Cordey and Bailly, 2007).

65 While previous geochronological works focused on the emplacement and crystallization of
66 magmatic rocks, the present study aims at distinguishing the magmatic event by analyzing the zircons
67 of an albitite vein (CH4) and of a (meta-)gabbro (CH1) from the cooling event by analyzing the
68 various REE-bearing minerals associated with the metamorphism of this metagabbro. Using U-Pb
69 and trace elements results, we discuss the cooling rate of this gabbro massif by comparing ages
70 obtained with a simple thermal modeling, and conclude by using the chemical signature of titanite on
71 the nature of the fluids which can contribute to this cooling.

72 **Geological background**

73 On the SW ridge (crest) of Mont Chenaillet, a massif of gabbro forms a lenticular body from
74 (of) 50 to 150 m thick and nearly 2 km long. It is intrusive into the serpentinites and sometimes
75 directly overlain by the pillow lavas (Figure 2). According to Manatschal et al. (2011), the contact
76 between the serpentinites/gabbros and the lavas is defined by a detachment fault along which the
77 serpentinites/gabbros were exhumed at the seafloor level before the emplacement of lavas flows. The
78 latter are fed by a few basaltic dikes that crosscut both gabbros and serpentinites. The voluminous
79 volcanic complex was built later than the gabbroic complex: basalts and gabbros have been suggested
80 to originate from the same magma source, but the plutonic system do not contribute to the volcanic
81 complex (Bertrand et al., 1987).

82 The lithology of this gabbro massif itself is mostly composed of coarse-grained
83 clinopyroxene-rich gabbros but other lithologies such as troctolites, diorites and albitites, can be
84 found. Troctolites (or more accurately metatroctolites) and olivine gabbros mainly occur at the base
85 of the unit: the continuous transition between gabbros - olivine gabbros and troctolites suggests that
86 these rocks crystallised synchronously. Dolerites also occur as rare dykes or small massifs. Finally,
87 albitites form centimetric to metric dikes within the gabbro massif. One exception is a small
88 decametric massif in the serpentinites, at « la Cabane des Douaniers » locality, which has been dated
89 by Li et al. (2013). The entire ophiolitic massif recorded an oceanic seafloor metamorphism prior to
90 a low grade alpine metamorphism (Mevel et al., 1978 ; Bertrand et al., 1987).

91 **Lithology and petrography of the gabbroic rocks**

92 Petrography of the gabbros *stricto sensu* is diversified. The magmatic ophitic textures is
93 locally affected by high temperature ductile shearing (Caby 1995) and the deformation is
94 heterogeneous. Gabbros are coarse- to fine-grained and the variation in crystal size can be sharp

95 (Figure 3). These sharp boundaries could indicate possible replenishments or re-injections of magma
96 at different stages of the gabbro crystallisation/cooling evolution.

97 Here we describe three typical samples of gabbros s.s. and one metatroctolite representative
98 of the massif. The samples CH1 and CH4 were collected from the SW ridge of the Mont Chenaillet,
99 on the centre of the gabbro lens (44°53'53" N ; 6°44'3.35"E); the CH3 sample comes from the
100 northern margin of the gabbro massif, in contact with the serpentinites, next to an oceanic detachment
101 fault (44°54'26.5" N ; 6°43'48.55"E; Figure 1). In the following, we only describe the petrography of
102 the metatroctolite (CH5) but will not present chemical analyses related to it. This sample is important
103 to understand and discuss the fluid origins affecting the gabbro massif. The mineralogical
104 assemblages are listed in the Supplementary data_1.

105 Sample CH4: The rock is an undeformed gabbro crosscuts by a centimetric thick vein of
106 albitite. The gabbroic part of the sample is coarse-grained with an ophitic texture. Clinopyroxene and
107 plagioclase are the main minerals and are centimetric in size. Clinopyroxene are sometimes rimmed
108 by a thin corona of brown amphibole (<0.1mm).

109 The albititic vein present in the sample has an irregular and diffuse contact with the gabbro,
110 suggesting that the melt feeding the felsic vein intruded the gabbro when it was not completely soli-
111 dified. It is mostly made up of albitic plagioclase, apatite, ilmenite, rare epidote and chlorite. Brown-
112 green amphibole crystals representing the only ferromagnesian mineral (Table 1) in this vein, are rare.
113 Some euhedral and cracked zircon crystals of several hundred micrometers in size also occur (ca-
114 thodoluminescence image in Figure 11b). -Late fractures filled with epidote and actinolite crosscut
115 the rock.

116 Sample CH3: This sample is collected on the strongly deformed edge of the gabbro at the top
117 of the lens which is in contact with the serpentinites, just below the oceanic detachment fault (near

118 section I of Manatschal et al., 2011; Figures 2 and 4). The gabbro has been metamorphosed at granu-
119 lite/amphibolite conditions as indicated by dark brown amphibole as the main ferromagnesian mineral
120 and minor clinopyroxene. Centimetric porphyroclasts of brown amphibole are wrapped by a well-
121 developed foliation (Figure 4). This brown amphibole is deformed and mantled by light brown and
122 green coronitic amphiboles. The light brown amphiboles are associated with ilmenite (Figure 5),
123 while the green amphiboles are associated with titanite (Figure 6). Rutile exsolution lamellae has been
124 observed within titanite and are related to the replacement of ilmenite. Finally, another generation of
125 titanite occurs in late fractures. Plagioclase is often recrystallised in an aggregate of fine crystals of
126 sodium-rich compositions close to albite (Table 1). When present, clinopyroxene is also surrounded
127 by a corona of dark brown to light brown and green zoned amphiboles, similar to that of the surround-
128 ing amphiboles. Contrary to the undeformed CH4 sample, the abundance of amphiboles highlights
129 that this sample is heavily amphibolitized.

130 Sample CH1: The rock is affected by anastomosed high temperature ductile shear zones
131 marked by the development of a pronounced metamorphic layering, consequently the rock can be
132 defined as metagabbro. The mineralogical association is mainly made up of clinopyroxene, brown to
133 green amphibole and plagioclase rich in albitic end member (Table 1). Accessory minerals are apatite,
134 ilmenite, titanite (Figure 8), cracked zircon crystals (cathodoluminescence image in Figure 12a) and
135 a few monazite (Figure 8c) and xenotime crystals (Figure 8d). It is worth noting that feldspar is black
136 with a dusty appearance: it is replaced by a fine aggregate of epidote, albite-oligoclase, +/-chlorite
137 corresponding to the prehnite – pumpellyite metamorphic facies. The metagabbro exhibits coronitic
138 texture similar to CH3 sample. However more complex textures can also be observed (Figure 7).
139 From clinopyroxene to plagioclase, clinopyroxene–brown amphibole symplectites replace the por-
140 phyroclasts of magmatic clinopyroxene (CpxMag). This pyroxene is recrystallised into an aggregate
141 of neoblastics clinopyroxene with brown hornblende (Cpx2 + bHbl) in a granulite metamorphic fa-
142 cies conditions. Then, a single brown amphibole gradually changes to a green hornblende (gHbl) and

143 corresponds to an amphibolite facies stage. The green hornblende is finally progressively replaced by
144 actinolite with associated chlorite and epidote (Act+Chl+Ep) corresponding to the greenschist facies..

145 In this sample, a millimeter wide shear zone is identified and contains a string of titanite +/-
146 ilmenite, monazite and xenotime grains surrounded by green amphibole and plagioclase (Figure 8).
147 Mineral textures reveal three titanite populations in this rock: (1) titanite associated with the green
148 coronitic amphibole (Figure 6) (2) titanite associated with other accessory minerals in the tiny ductile
149 shear zone (Figure 8) and (3) titanite recrystallised with rutile, after ilmenite (Figure 9).

150 Sample CH5 : Metatroctolites are abundant on the few tens of meters at the base of the massif.
151 The ferromagnesian minerals are largely dominant over the plagioclase. Another notable outcrop from
152 which the sample CH5 (Figure 10) was collected is located on the middle of the SW ridge of the Mont
153 Chenaillet. In all these rocks, olivine is always absent and is replaced, at the contact with plagioclase
154 by a coronitic aggregate composed of amphibole (tremolite) enclosed by a chlorite rim. Rare
155 clinopyroxene, brown and/or green hornblendes and oxides can also be found.

156 **Analytical techniques**

157 **Electron probe microanalysis (EPMA)**

158 Titanite and monazite were analysed for major and minor elements with an EPMA CAMECA SX100
159 at Laboratoire Magmas et Volcans (LMV). For titanite, analyses were made with an accelerating volt-
160 age of 20kV and a 40 nA beam current. The crystals used for analysis were PET for Ca, Ce and S,
161 TAP for Si, Na and Y, LPET for P, Cl, La and Sr, and PC0 for F and O. For monazite, analyses were
162 made accelerating voltage of 15kV and a 40 nA beam current. The crystals used for analysis were
163 PET for Ca, Si, La, Th, U and Ce, LPET for P, Y and Pb, and LLIF for Pr, Nd, Sm and Gd. Several
164 trace elements in these minerals were also analysed for comparison with laser ablation ICP-MS (LA-
165 ICPMS) data or when these minerals were too small. The different mineral studied in this contribu-
166 tion were imaged for back-scattered electrons (BSE) using this microprobe.

167 **Laser ablation-inductively coupled plasma mass spectrometry (LA-ICP-MS)**

168 *Trace element analyses*

169 Trace element analysis of titanite was done by laser ablation-inductively coupled plasma mass
170 spectrometry (LA-ICP-MS) using a Thermo Element XR coupled to a 193nm excimer laser
171 (Resonetics Resolution M-50E) at LMV. The spot size was 20 μm with a repetition rate of 1 Hz and
172 a fluence of 3 J/cm². We purposely set a low frequency to avoid drilling through titanite too quickly.
173 Each run lasted 20 seconds of background acquisition plus 90s of analyses. Each sequence was brack-
174 eted by two analyses of GSE-1G or GSD-1G standards at the beginning and at the end of the sequence
175 (Jochum et al., 2005). Khan titanite reference material (Heaman, 2009) was regularly analysed
176 throughout the analytical session to monitor data quality at the same spot size as the analysed un-
177 knowns to account for downhole fractionation. Hf content was monitored during analysis of titanite
178 in order to identify potential micro inclusions of zircon. All analyses with Hf content above the back-
179 ground values were discarded. Internal normalisation for LA-ICP-MS data was done using ⁴³Ca and
180 data processing was conducted using the GLITTER software (Griffin, 2008).

181 *U-Pb dating*

182 Zircon, monazite, titanite and xenotime have been analysed in thin section by LA-ICP-MS (La-
183 boratoire Magmas et Volcans, Clermont-Ferrand, France) in order to control the position of the grain
184 relative to the textures observed in the sample. These minerals were ablated under pure He using a
185 Resonetics Resolution M-50 system equipped with a 193 nm Excimer laser coupled to a Thermo
186 Element XR sector field ICP-MS using a jet interface high-capacity pumping device for zircon and
187 titanite or an Agilent 7500 cs quadrupole ICP-MS equipped with a dual pumping system for monazite
188 and xenotime. N₂ was supplemented to Ar and He carrier gas for sensitivity enhancement (Paquette
189 et al., 2014). The laser operated with a spot diameter of 27 μm , a repetition rate of 3 Hz, and a fluence

190 of 2.5 J/cm² for zircon and titanite and a spot diameter of 9 μm, a repetition rate of 1 Hz, and a fluence
191 of 4.0 J/cm² for monazite and xenotime, respectively.

192 The instruments were tuned to maximise the ²³⁸U intensity and minimise ThO⁺/Th⁺ (<1%) using
193 the NIST SRM 612 glass. Background levels were measured on-peak with the laser off for ~30 s,
194 followed by ~60 s of measurement with the laser firing and then ~10 s of washout time (Huray et al.
195 2010). Reduction of raw data was carried out using the GLITTER® software package (van Achter-
196 bergh et al. 2001). Isotope ratios were corrected for laser-induced and instrumental mass fractionation
197 via sample-standard bracketing using the GJ-1 zircon reference material (Jackson et al., 2004) for
198 zircon and titanite (Fallourd et al., 2014) and the Trebilcock monazite reference material (Tomascak
199 et al., 1996) for monazite and xenotime, respectively. The ²³⁵U signal is calculated from ²³⁸U based
200 on the ratio ²³⁸U/²³⁵U = 137.818 (Hiess et al. 2012). The 91500 zircon reference material (Wiedenbeck
201 et al. 1995) and the Itambe and Bananeira monazites (Goncalves et al., 2016) were analysed along
202 with the samples to independently monitor the external precision and accuracy of the measurements.
203 Common Pb was not corrected owing to the large isobaric interference of ²⁰⁴Hg. Concentrations of
204 U, Th, and Pb were calculated by normalisation to the certified composition of GJ-1 reference mate-
205 rial. ²⁰⁷Pb/²⁰⁶Pb versus ²³⁸U/²⁰⁶Pb diagrams (Tera and Wasserburg 1972) were generated using
206 Isoplot/Ex v. 2.49 software package by Ludwig (2001). Error ellipses for each point are quoted at the
207 2σ level.

208 **Results**

209 **Mineral chemistry and Geothermometry**

210 The metamorphic minerals are brown to green amphiboles and actinolite, epidote, albite –
211 oligoclase, chlorite, ilmenite, titanite and titanite-rutile (after ilmenite). In the classification for
212 calcium amphiboles by Leake et al (1997), amphiboles ranged as magnesio-hornblendes and
213 actinolites (Table 1). The colour of the amphibole, brown to green, depends on the titanium content

214 of the mineral. Primary brown hornblende of sample CH3 is rich in titanium and range in composition
215 between 2.5 and 3 wt% TiO₂. On the other hand, coronitic light brown hornblende TiO₂ content is
216 around 1.50 wt% while below 0.40 wt% for green amphibole. The concentrations of brown and green
217 hornblende located in coronas of CH1 metagabbro are 2.66-1.90 wt% and around 0.40 wt%
218 respectively. In this sample, green actinolite of the tiny shear zone which contains the string of titanite
219 +/-ilmenite, monazite and xenotime has similar low values TiO₂ (\approx 0.40 wt%). Finally, in CH4
220 sample, TiO₂ concentrations in the green hornblendes of the albititic vein are 1.50-1.60 wt%. Brown
221 hornblendes, light brown hornblendes, green hornblendes, actinolite are progressively less and less
222 rich in this element. Overall, the composition of plagioclase is very acidic in all rocks: it ranges from
223 albite to oligoclase (Table 1).

224 Provided that a titaniferous buffer mineral as titanite, ilmenite or rutile is present, the change
225 from brown to green amphibole reflects a decrease in the concentration of this element and of the
226 temperature. The concentration of Ti is temperature-dependent and can be used as a robust
227 geothermometer (Otten, 1984; Ernst et Liu, 1998; see below). In a first approach, the brown to green
228 colors of the hornblendes are good qualitative thermometric indicators and reflect respectively high
229 to low temperature conditions of the granulite and amphibolite facies; actinolite is evidence of
230 greenschist facies conditions.

231 Temperature estimates were acquired by applying amphibole-based geothermometers. We
232 used the hornblende-plagioclase geothermometer of Holland and Blundy (1994; edenite-tremolite
233 calibration) and the amphibole-only thermobarometers by Ernst and Liu (1998) and Putirka (2016).
234 We previously noted that the mineralogical assemblages in a single rock are not always in equilibrium
235 and record different stages of the thermal history of the massif. Accordingly, the hornblende-
236 plagioclase geothermometer must be used with caution and the equilibrium between the mineral pairs
237 must be carefully checked. On the other hand, geothermometers only based on the amphibole
238 composition do not have this drawback. The semi-quantitative amphibole thermobarometer of Ernst

239 & Liu (1998) is based on Ti content of the M2 site that increases with temperature. The use of Ti
240 thermometer requires an excess of Ti in the system: we assume that this condition is satisfied because
241 ilmenite and/or titanite are always present. The accuracy of this thermometer has been estimated at
242 the Institut für Mineralogie of Hannover (Germany) using published and unpublished experimental
243 data (J. Koepke, pers. Comm.). The equation of this geothermometer is given in France et al. (2021).
244 For the amphibole-only thermobarometer of Putirka (2016), we used equation 6 with a lithostatic
245 pressure of 0.2 Gpa, which is compatible with the depth of gabbro emplacement in a crust formed at
246 slow spreading ridges (e.g. Canales et al. 2017). In any case, equation 6 of the Putirka thermometer
247 is almost insensitive to small pressure changes ($2.4^{\circ}\text{C}/0.1\text{ GPa}$). It has to be noted that, the amphibole-
248 only thermobarometer of Putirka, (2016) was calibrated for igneous systems with $T > 650^{\circ}\text{C}$ and
249 therefore is preferably suitable for estimating temperature conditions from igneous and high-grade
250 metamorphic rocks (Molina et al., 2021).

251 Temperatures obtained for the two samples CH1 and CH3 with both amphibole-only
252 thermometers for brown amphiboles are consistent and vary between 950°C and 850°C (Table 1). On
253 the other hand, the hornblende-plagioclase geothermometer using brown amphibole gives lower
254 results ($790\text{-}820^{\circ}\text{C}$, Table 1). This discrepancy between the amphibole-only and the hornblende-
255 plagioclase geothermometers can be explained by the fact that plagioclase of acidic composition is
256 no longer in equilibrium with high temperature Ti-rich amphiboles. In general, the temperatures
257 recorded by all geothermometers using green amphiboles are lower (between 800°C and 550°C ; Table
258 1). For the entire range of green hornblende compositions, Ti-in amphibole thermobarometer of Ernst
259 and Liu (1998; « revisited » by Koepke) and the hornblende-plagioclase geothermometer give
260 equivalent results. However, the Putirka's amphibole-only thermometer (2016) tends to give higher
261 estimates and overestimates the temperatures of amphibolite and greenschist facies conditions
262 Consequently, we did not apply it to the amphiboles of the greenschist facies.

263 In the CH3 sample, oikocrysts of Ti-rich amphibole indicate temperatures between 880°C-
264 910°C (therm. Purtika) and 950°C (therm. Ernst et Liu, 1998 « revisited ») (brown amphiboles in
265 Figures 5 and 6; Table 1). Their formation occurs at a late-magmatic stage prior to retrograde meta-
266 morphism. The light brown coronitic amphibole, located around the brown primary amphibole and
267 contemporary to the ductile deformation, indicates temperatures around 800-750°C(therm. Ernst et
268 Liu, 1998 « revisited »), 800-830 (therm. Purtika) and 730-750°C (therm. Holland and Blundy; Fig-
269 ure 5 and Table 1). This highlights that deformation immediately followed the emplacement and the
270 crystallisation of the gabbro. The light-brown- to green amphibole coronas record decreasing temper-
271 atures from 800°C (Figure 5) down to 550°C (Figure 6).

272 In the remarkable assemblage around the clinopyroxene of the CH1 sample, temperatures
273 range from 870°C to 570 °C (Figure 7). In the amphibolitic layer containing the string of titanite,
274 monazite, ilmenite and xenotime (Figure 8), we note the consistency of the temperatures obtained
275 with hornblende –plagioclase geothermometer (550-600°C) and those acquired with the Ti-amphi-
276 bole thermobarometer of Ernst and Liu (1998) (550-600°C). These are the temperatures of the am-
277 phibolite-greenschist transition around 550-600°C as attested by the actinolite + plagioclase paragen-
278 esis.

279 According to the amphibole geothermometry, the crystallisation temperature of the albitite
280 vein is around 760 and 780°C (therm. Ernst et Liu, 1998 « revisited »), 815°C (therm. Purtika; Table
281 1).

282 **Trace elements in titanite**

283 In CH1, three types of titanite in different textural context were analysed : (1) titanite cristal-
284 lising in the green hornblende corona at the expense of the Ti-rich brown amphibole, (2) titanite
285 crystallising at the expense of ilmenite (Figure 9) and (3) titanite associated with the string of acces-
286 sory minerals in a tiny ductile shear zone (Figure 8). In Figure 11a, a diagram reporting Y vs. Nb

287 reveals that these three types of titanite are chemically different. Types 1 and 2 have lower Nb and Y
288 contents ($145 < \text{Nb} < 1982$ ppm and $80 < \text{Y} < 18328$ ppm, respectively), while type 3 has high Nb and Y
289 contents ($2764 < \text{Nb} < 5158$ ppm and $19163 < \text{Y} < 29017$ ppm, respectively). Type 3 has overall much-
290 richer trace elements content than types 1 and 2 (Table 2 and supplementary data_2). In CH3, titanite
291 located within the green amphibole corona (type 1) have the same chemical characteristics as for CH1
292 sample (Table 2 and supplementary 2). In CH3, another type of titanite (type 4) occurs in late frac-
293 tures. Although most trace elements in type 4 have fairly similar content to types 1-2 (Table 2 and
294 supplementary data_2), it has generally higher Nb, Cr, V and Sn contents (77-250 ppm, 47-118 ppm,
295 353-594 ppm and 35-97 ppm) than type 1 titanite (24-111 ppm, 9-97 ppm, 247-480 ppm and 15-35
296 ppm respectively).

297 Chondrite-normalised REE patterns (Figure 11b) also distinguish the different types of titan-
298 ites described above: type 1 titanites from CH3 sample have low REE content, rather flat patterns and
299 moderate positive to negative Eu anomalies. In contrast, type 3 from CH1 sample corresponding to
300 titanite from the accessory mineral of the ductile shear (Figure 8), define a tight group 20-200 times
301 richer in REE content, with quite flat REE patterns and a strong negative Eu anomaly (Figure 11b ,
302 Table 2 and supplementary data_2). Notably, type 3 titanite define a tight group of analyses in a
303 Chondrite-normalized diagram while the other titanite types analyses are more scattered. Finally type
304 4 titanites from sample CH3 display similar REE patterns to those of type 1 from the same sample
305 but with a marked positive Eu anomaly. Type 4 titanite texturally occurs in late fractures and Eu
306 anomaly in this titanite type is most probably inherited from late fluid circulation and local feldspar
307 alteration.

308 **U-Th-Pb geochronology**

309 *Ages of the magmatism recorded by zircon*

310 The zircons from the CH1 gabbro and the CH4 albitite vein allow dating the crystallisation
311 and the emplacement of the massif. The zircon crystals of the gabbro CH1 are 30–100 μm long,
312 subhedral and sometimes cracked. Cathodoluminescence images (Figure 12a) show oscillatory
313 zoning: such internal structure is well consistent with those of zircons crystallised from mafic magmas
314 (Corfu et al 2003, Paquette et al., 2017). In the metagabbro, U and Th contents are very variable, from
315 9 to 342 ppm and from 2 to 130 ppm, respectively, whereas the Th/U ratios also yield magmatic
316 values, ranging from 0.10 to 0.49. Reported in a Tera-Wasserburg diagram, thirty-four of the thirty-
317 five analysed points plot on a discordia line which allows to calculate a lower intercept age of 161.0
318 \pm 0.8 Ma (Fig.12a).

319 In the albitite vein (CH4), several crystals form rectangular half-millimetre tablets with square
320 or diamond-shaped cross-sections. Slight localised alteration along fractures is noticeable in
321 cathodoluminescence (Figure 12b). However, the network of these fractures is sufficiently spaced to
322 allow analyses by laser-ICPMS. The U and Th contents of zircons from CH4 are very low, from 8 to
323 31 ppm and from 2.8 to 19.5 ppm, respectively, in agreement with a mantle-derived source. The Th/U
324 ratios ranging from 0.36 to 0.65 display typically magmatic values (Table 3). Reported in a Tera-
325 Wasserburg diagrams, the seventeen analytical points define a discordia line which yields a lower
326 intercept at 161.8 \pm 1.7 Ma (Figure 12b).

327 Both dates, 161.8 \pm 1.7 Ma and 161.0 \pm 0.8 Ma, attest of the age of the emplacement of
328 the gabbroic massif and associated rocks.

329 *Ages of the cooling recorded by the metamorphic chronometer minerals: monazite, xenotime*
330 *and titanite*

331 All three metamorphic chronometer minerals, monazite, titanite and xenotime are found in a
332 tiny shear zone in sample CH1. They date this shearing event which occurs during the cooling of the
333 gabbro when this one reached the greenschist facies conditions. A cluster of a few rounded grains

334 (around ten) of monazites ranging in size from 5 to 20 microns is associated with the string of titanite
335 and ilmenite. (Figure 8c). Composition of monazite is relatively homogeneous. UO_2 contents are low
336 and vary between 0.15 and 0.42 %, while ThO_2 varies from 1.36 to 5.06 % (Table 3).

337 Four small grains of xenotime are included in the string. Only a single grain of 50x30 microns
338 size could be analysed for dating. (Figure 8d).

339 We noted previously that three populations of titanite can be distinguished by their
340 petrographic textures and their compositions in the sample CH1 (Table 2 and supplementary data_2).
341 Crystals associated with green Hbl + Pl coronas around Cpx/brown hornblende and rare crystals
342 scattered in the rock are poor in trace elements (Figure 6). Those included in the string of titanite +/-
343 ilmenite associated to monazite and xenotime grains and located in a millimetric amphibolitic layer
344 (Figure 8) are rich in trace elements (Table 2 and Figure 11). Their fairly high Th and U contents (up
345 to 222 ppm and 187 ppm respectively) allow dating of these minerals.

346 The analytical points of the U-Pb dating of the three minerals: monazite, xenotime and titanite
347 plot along discordia lines and yield lower intercept ages at 161.3 +/-4.0 Ma, 161.5 +/-2.4 Ma and
348 158.4 +/-2.3 Ma, respectively (Figure 13). These three ages are consistent within the analytical
349 uncertainties.

350 **Discussion: Retrograde evolution of the (meta)gabbro of Mont Chenaillet -** 351 **Dating and modeling the cooling**

352 **Metamorphism and cooling of the gabbro**

353 In the Mont Chenaillet massif, isotropic gabbros, foliated metagabbros and amphibolites
354 coexist, showing that deformation and metamorphism are unevenly distributed. The petrographic
355 relationships in the studied rocks show a chronology in the crystallisation of the amphiboles,
356 gradually passing from brown to green, then to actinolite, this evolution being documented in the

357 Figure 7. The mineral assemblages are consistent with peritectic reaction as clinopyroxene + melt +
358 fluid \rightarrow amphibole + plagioclase and the hydrothermal metamorphic reactions: clinopyroxene +
359 calcic plagioclase + fluid \rightarrow amphibole (+ clinopyroxene 2) + sodic plagioclase and dark brown-
360 amph + An-rich Pl1 = light brown amph /green amph + Ab rich Pl2 + ilmenite/titanite. In
361 metatroctolite outcrops, the absence of olivine supposes the involvement of the reaction olivine +
362 plagioclase + fluid = tremolite + chlorite (Figure 10). These amphibole-forming reactions were
363 continuously retrogressive and they testify that the different rocks record the cooling history of the
364 massif. These minerals are, however, unevenly distributed throughout the whole massif. This requires
365 a pervasive and continuous infiltration of aqueous fluids/hydrated melt over time but which are more
366 or less channelised.

367 In this contribution, we aimed at dating different minerals testifying of the magmatic (zircon)
368 and cooling history (monazite, titanite, xenotime). The dates recorded in the zircon, 161.8 +/- 1.7 Ma
369 and 161.0 +/- 0.8 Ma, constrain the age of the emplacement of the gabbroic massif and associated
370 rocks. They are similar within uncertainties with those published in Li et al. (2013). They are con-
371 sistent with the ages of the oceanic sediments of the Lago Nero-Replatte unit, the neighbouring oph-
372 iolite body which contains radiolarites providing a middle bathonian age between 166 and 162 Ma.
373 (Cordey and Bailly, 2007). On the other hand, the three metamorphic minerals, monazite, titanite and
374 xenotime (belonging to the greenschist paragenesis of the tiny shear zone of sample CH1) crystallised
375 between 550 and 600°C and thus date the transition from amphibolite facies to greenschist facies
376 during the cooling of the gabbro. The three ages obtained: 161.3 +/-4.0 Ma, 161.5 +/-2.4 Ma and
377 158.4+/-2.3 Ma, respectively (Figure 13) are consistent within the analytical uncertainties. Unfortu-
378 nately, the ages achieved by the different mineral chronometers: zircon for the magmatic episode,
379 monazite, titanite and xenotime for the metamorphic one, between 161 and 158 Ma, are similar within
380 the analytical uncertainties and do not allow to specify the chronology of this cooling from magmatic
381 temperatures to those of the greenschist facies (550 - 600°C). This attests that the magmatism and the

382 metamorphism associated with the cooling of the magmatic rock follow one another in a very short
383 time.

384 The metagabbros also present very low temperature mineral assemblages (Prehnite-
385 pumpellyite facies), such as the fine alteration of plagioclase in epidote and albite (Figure 7), and
386 maybe the alteration of ilmenite into titanite + rutile (Figure 9), or else some minerals in tension
387 cracks. We agree with Mevel et al. (1978) and Bertrand et al. (1987) that this very low temperature
388 event is difficult to date. It is still unclear whether they record the end of the cooling of the gabbro,
389 contemporaneously with the serpentinisation of the surrounding peridotites or if they are linked to the
390 obduction of the ophiolite and the alpine collision.

391 **Modelling the crystallisation and cooling of the (meta)gabbro of Mont Chenaillet**

392 In order to assess the duration of the cooling process, we have established simple conductive
393 thermo-kinetic models to reproduce the thermal evolution obtained with the petrologic study. The aim
394 is to estimate the thermal evolution and the lifespan of the crystallisation and cooling of a 150 m thick
395 gabbroic lens. The key question is: Which duration is required to solidify it? We used a transcription
396 for PC of the CONTACT program (Peacock, 1989; Spear, 1989; Spear & Peacock, 1990; Spear et al.,
397 1991) that simulates contact metamorphism by using an explicit finite difference algorithm to solve
398 the one-dimensional heat transfer from an intrusion to the intruded host rock. The model supposes
399 some simplifications: the igneous body is instantaneously intruded and we do not take into account
400 advective heat transfers during the ascent of magma from the underlying reservoir. Heat transfers
401 only proceeds by conduction while hydrothermal circulation in the gabbro (attested by the abundance
402 of hydrated minerals) enables a fast heat transfer (e.g. Zhang et al., 2014). The model assumes a single
403 injection without replenishment of the magmatic lens. In the studied case, this condition seems to be
404 more or less satisfied, as evidenced by the scarcity of intrusive contacts of gabbro in gabbro (Figure
405 3), or between the different lithologies : troctolite – gabbro – plagiogranites (diorite and albitites),
406 thus suggesting a limited replenishment or reinjection of the magmatic lens.

407 Thermodynamic constants have been selected following Spear & Peacock (1990), Cannat et
408 al. (2004), Leshner & Spera (2015) and Gillis & Coogan (2019) with a thermal conductivity of 3.0
409 W/m/K, a rock density of 3000 kg/m³, a specific capacity of 1200 J.kg/K and a latent heat of
410 crystallisation of 400 kJ/kg. We set the liquidus at 1200°C, a realistic temperature for a relatively
411 primitive basaltic melt, and an almost dry solidus around 1050°C. According to Escartin et al (2003)
412 and Manatschal et al. (2011) the gabbros are intrusive in very shallow levels in a cold lithosphere at
413 the brittle-ductile transition. If the gabbro is exhumed along an oceanic detachment fault, the
414 temperature of the surrounding rocks has changed progressively during the exhumation since the
415 emplacement in a high temperature environment to the seafloor. This variation of temperature during
416 the exhumation and the rate of this exhumation will determine the cooling rate of the gabbro.
417 Consequently, we chose an average fixed temperature of 550°C for the surrounding rocks which
418 corresponds to the estimated temperature of the tiny ductile shear zone containing the three
419 chronometer minerals: titanite, monazite, and xenotime (Figure 8)

420 Our straightforward thermal modelling predicts that the magmatic lens is completely
421 solidified in about 350 years and cooled to 550-600°C in less than 8000 years (Figure 14). If the
422 cooling started in a warmer environment, in the range of 750-700°C, and then gradually decreased,
423 this would only change our result by a factor of 3 or 4. However, as already highlighted, the cooling
424 of the Mont Chenaillet gabbro takes place in a context of strong hydrothermal convection and
425 therefore these estimates using such conductive thermal models can only be maximum. These surely
426 greatly overestimate the time of cooling. Nevertheless and despite the uncertainties of this calculation,
427 these models give an order of magnitude of the cooling time of a gabbro massif like that of Mont
428 Chenaillet. They are in agreement with the proposals of Escartin et al. (2003) who suggest that the
429 distribution and duration of gabbro emplacement had to be limited in space and time. Although the
430 cooling rates estimated by Coogan et al (2007) or Faak and Gillis (2016) are lower than our results,
431 these authors demonstrate that the cooling of gabbros in the oceanic crust is very fast. On the contrary,

432 the cooling rates considered by Zhang et al (2013) are significantly higher in the context of a vigorous
433 hydrothermal circulation. In a similar way, Mc Caig et al (2010) suggest that hydrothermal discharge
434 along detachment fault favours rapid cooling of the gabbros). In all cases, our estimations are far
435 below the analytical uncertainties of our geochronometers and nicely explain why we cannot resolve
436 the different stages of the cooling history ages with this method.

437 **Two origins for the sources of water**

438 The multiple generations of hydrated minerals crystallising throughout the retrograde thermal
439 evolution from the late-magmatic stage (sample CH3: 950°C) are evidences of a permanent, albeit
440 irregularly distributed, volatile-bearing agent - rock interaction during multiple fluid infiltration
441 events: brown and green amphiboles and the pervasive low temperature alteration of plagioclase to
442 albite + epidote. Another example of water-rock interaction in the Chenaillet massif is the complete
443 transformation of the troctolite olivines to chlorite and tremolite (Figure 10). Coogan et al. (2001),
444 Persev et al. (2015) and Harigane et al. (2019) well summarised the various sources of water that can
445 lead to the hydration of the oceanic crust: (a) a residual hydrous silicate melt derived from the
446 fractionation of basalt, (b) an exsolved magmatic fluids from such a hydrous silicate melt, (c)
447 seawater-derived fluids and finally mixtures of these end-members.

448 In the gabbroic massif of Mont Chenaillet, the scarcity of the differentiated facies (ferro-gab-
449 bros, diorites and plagiogranites) precludes the assumption that water of magmatic origin was the sole
450 cause of the significant hydration of the gabbro lens. On the other hand, the high amount of amphibole
451 in the CH3 sample close to the detachment fault, which represents a preferential channel for the cir-
452 culation of the seawater, strongly suggests the major role of seawater-derived fluid in the metamor-
453 phism of the massif. The extensive alteration of the olivines in the metatroctolites suggests a wide-
454 spread hydration of these rocks (Figure 10). However, the detailed study of the chemistry of titanite
455 and the fact that their textural context is linked with very different chemical compositions (Figure 11)

456 suggest an infiltration of fluids of various nature and hydrous melts. More specifically, type 3 titanite
457 found within a ductile shear in sample CH1 (Figure 8) have high contents in trace elements (e.g. REE,
458 Nb, Ta, Table 2). Their compositions are characteristics of a felsic melt (Protwake and Klemme, 2005;
459 Hoskin et al., 2000; Bruand et al., 2014). These signatures of the titanite of the ductile shear are very
460 different from the other titanites both found in CH1 and CH3. Indeed, type 1, 2 and 4 have much
461 lower content in trace elements and REE in particular (Table 2 and Fig11). Titanite 1 and 2 chemical
462 signatures are inherited from the reaction of previous Ti-bearing phases (Ti-rich Amphibole for type
463 1 and ilmenite for type 2) and are directly linked to changing metamorphic conditions from granulite
464 toward the amphibolite/greenschist facies. Type 4 was only found in late fractures affecting Ch3
465 samples and its chemistry (low REE content and positive anomaly) is most likely linked to the late
466 circulation of fluid altering feldspar. Some authors (eg. Persev et al., 2015) have suggested that local
467 enrichment in trace elements of the gabbros (REE, Y, Nb, ...) could originate from exsolved magmatic
468 fluids released by hydrous felsic melts such as plagiogranites during their crystallisation. Tribuzio et
469 al, (2019) recently proposed that the small gabbro massif of Rocher de l'Aigle (north of Mont Che-
470 naillet) would be metasomatised by felsic hydrous melt feeding the dykes of albitite. It has to be noted
471 that no intrusive veins at the outcrop scale could be found associated to the micro shear zone in sample
472 CH1. Therefore, instead, the trace element abundance of the type 3 REE-rich titanite (Figure.11b) in
473 this micro shear zone could originate from a metasomatic fluid resulting from the crystallisation of a
474 SiO₂-rich hydrous melt feeding the veins of albitite and percolated into the already partially cooled
475 gabbro. The varied composition of the other titanite types suggests a diversity of fluid sources. As we
476 are in a context of vigorous hydrothermal circulation in an oceanic crust, a seawater-derived hydro-
477 thermal fluid origin of the principal source of water responsible for the overall hydration of the massif
478 is a reasonable hypothesis during the exhumation of the gabbro along the detachment shear zone.
479 Tribuzio et al. (2019) do not preclude such an origin as they write: “we cannot exclude, however, that
480 some of the amphibole (and clinopyroxene) chemical variability reflects replacement and/or over-
481 growth by a secondary amphibole in response to interaction of the gabbros with fluids, which could

482 be exsolved from the melt trapped within the deformed gabbros, and/or derived from seawater during
483 subsequent exhumation of the gabbros to the seafloor.”

484 **Conclusions**

485 Multiple generations of metamorphic minerals and specially amphiboles are evidence that the
486 gabbro petrographically records different steps of its cooling during exhumation to the seafloor along
487 an oceanic detachment fault, suggesting that the rock underwent separate episodes of fluid/rock
488 interaction and/or deformation. The timing of this cooling could be theoretically measured using in
489 situ dating on thin section in textural context of the chronometer minerals linked to this
490 metamorphism by LA-ICPMS. The crystallisation age of the gabbro is determined by U-Pb zircon
491 dating at 161.0 +/- 0.8 Ma similar to this obtained in the albitic vein at 161.8 +/- 1.7 Ma, whereas the
492 metamorphic minerals, monazite (161.3 +/- 4.0 Ma), titanite (158.4 +/-2.3 Ma) and xenotime (161.5
493 +/- 2.4 Ma) in a tiny ductile shear zone date a shearing event during the cooling of the gabbro at the
494 transition of the amphibolite and greenschist facies. Unfortunately, the different minerals display
495 similar ages within the analytical uncertainties and the cooling age cannot be distinguished from the
496 magmatic age of the massif. Indeed, a simple numerical model confirms that the crystallisation and
497 cooling of the Mont Chenaillet gabbro are extremely fast: the crystallisation happens in a few hundred
498 years and the cooling is completed in a few thousand years. In this way, we show strong evidence for
499 rapid exhumation and cooling of the gabbro related to detachment faults in the Chenaillet ophiolite
500 generated in a slowly spreading accretionary system. Even if the cooling age cannot be resolved with
501 the geochronology, the petrological work and the various chemical compositions recorded in titanite,
502 nicely highlighted that the development of this retrograde metamorphism required multiple fluid (and
503 possibly hydrous SiO₂-rich melts) infiltration events enhanced by multiple ductile/brittle deformation
504 events during the exhumation. We propose two origins for the source of water : pervasive seawater-
505 derived fluids and more locally, exsolved magmatic fluids from evolved hydrous silicate melts
506 (plagiogranite veins) and infiltrated into the already partially cooled gabbro. Even if we have no

507 evidence, we cannot exclude that the gabbro could be locally metasomatised by felsic hydrous melt
508 feeding the dykes of albitite as suggested by Tribuzio et al. (2019) in the neighbouring massif.

509 **Acknowledgements** The co-Editor-in-Chief Nadia Malaspina, Maria Rosaria Renna and an
510 anonymous reviewer are thanked for their constructive comments. Thanks are due to Jean Luc
511 Devidal for his help in the use of EMPA. This is Laboratory of Excellence ClerVolc contribution
512 number 526.

513 **References**

514 Bertrand, J., Courtin, B., Vuagnat, M., 1982. Elaboration d'un secteur de lithosphère océanique li-
515 guro-piémontais d'après les données de l'ophiolite du Montgenèvre (Hautes-Alpes, France et pro-
516 vince de Turin). *Ofioliti* 7, 155–196.

517 Bertrand, J., Dietrich, V., Nievergelt, P., Vuagnat, M., 1987. Comparative major and trace element
518 geochemistry of gabbroic and volcanic rock sequences, Montgenèvre ophiolite, Western Alps.
519 *Schweizerische Mineralogische und Petrographische Mitteilungen Schweiz. Mineral. Petrogr. Mitt.*
520 67, 147–169.

521 Boynton, W. V.W.V., 1984. Cosmochemistry of the Rare earth Elements: meteorite studies *Cosmo-*
522 *chemistry of the rare earth elements: meteorite studies. Developments in Geochemistry Dev. Geo-*
523 *chem.* 63–114. doi:10.1016/b978-0-444-42148-7.

524 Bruand, EE., Storey, CC., Fowler, MM., 2014. Accessory mineral chemistry of high Ba-Sr granites
525 from Northern Scotland: constraints on petrogenesis and records of whole-rock Signature. *Journal*
526 *of Petrology J. Petrol.* 55, 1619–1651. doi:10.1093/petrology/egu037.

527 Caby, R., 1995. Plastic deformation of gabbros in a slow-spreading Mesozoic Ridge: example of the
528 Montgenèvre Ophiolite *Plastic deformation of gabbros in a slow-spreading Mesozoic Ridge:*

529 Example of the Montgènevre Ophiolite. In: Vissers, R.L.M., Nicolas, A. (Eds.), *Mantle and lower*
530 *crust exposed in oceanic ridges and in ophiolites* *Mantle and Lower Crust Exposed in Oceanic*
531 *Ridges and in Ophiolites*. Kluwer Academic Publishers, pp. 123–145.

532 Canales, J. P.J.P., Dunn, R. A.R.A., Arai, R., Sohn, R. A.R.A., 2017. Seismic imaging of magma
533 sills beneath an ultramafic-hosted hydrothermal system. *Geology* 45, 451–454.
534 doi:10.1130/G38795.1.

535 Cannat, M., Cann, J., MacLennan, J., 2004. Some hard rock constraints on the supply of heat to mid-
536 ocean ridges. *Mid-ocean Ridges: Hydrothermal Interactions between the Lithosphere and Oceans*.
537 American Geophysical, Washington, DC, pp. 111–149.

538 Chalot-Prat, F., 2005. An undeformed ophiolite in the Alps: field and geochemical evidence for a
539 link between volcanism and shallow plate tectonic processes. In: Foulger, G.R., Natland, J.H., Pres-
540 nall, D.C., Anderson, D.L.D.L. (Eds.), *Plates, Plumes and Paradigms*. Geological Society of Ame-
541 rica Special Papers, 388. pp. 751–780.

542 Coogan, L.A., Wilson, R.N., Gillis, K.M., MacLeod, C.J., 2001. Near-solidus evolution of oceanic
543 gabbros: insights from amphibole geochemistry. *Geochim. Cosmochim. Acta* 65, 4339–4357.

544 Coogan, L.A., Wilson, R.N.R.N., Jenkin, G.R.T.G.R.T., 2007. Contrasting cooling rates in the lower
545 oceanicCrust at fast- and slow-spreading ridges revealed by geospeedometry. *Journal of petrology*J.
546 *Petrol.* 48, 2211–2231.

547 Cordey, Fabrice, Bailly, Anthony, 2007. Alpine ocean seafloor spreading and onset of pelagic sedi-
548 mentation: new radiolarian data from the Chenaillet-Montgenève ophiolite (French-Italian
549 Alps)Alpine Ocean seafloor spreading and onset of pelagic sedimentation: new radiolarian data
550 from the Chenaillet-Montgenève ophiolite (French-Italian Alps). *Geodinamica Acta*Geodin. Acta
551 20 (3), 131–138. doi:10.3166/ga.20.131-138.

552 Corfu, Fernando, Hanchar, John M., Hoskin, Paul W.O., Kinny, Peter, 2003. Atlas of zircon tex-
553 tures. *Reviews in Mineralogy and Geochemistry* *Rev. Mineral. Geochem.* 53 (1), 469–500.
554 doi:10.2113/0530469.

555 Costa, S., Caby, R., 2001. Evolution of the Ligurian Tethys in the Western Alps: Sm/Nd and U/Pb
556 geochronology and rare-earth element geochemistry of the Montgenèvre ophiolite (France). *Chemi-
557 cal Geology* *Chem. Geol.* 175, 449–466.

558 Desmurs, L., Müntener, O., Manatschal, G., 2002. Onset of magmatic accretion within a magma-
559 poor rifted margin: a case study from the Platta ocean-continent transition, eastern Switzerland
560 Onset of magmatic accretion within a magma-poor rifted margin: a case study from the Platta Ocean-
561 continent transition, eastern Switzerland. *Contributions to Mineralogy and Petrology* *Contrib. Mine-
562 ral. Petrol.* 144 (3), 365–382.

563 Ernst, W. G.W.G., Liu, J., 1998. Experimental phase-equilibrium study of Al- and Ti-contents of
564 calcic amphibole in MORB—A semiquantitative thermobarometer. *American Mineralogist* *Am. Mi-
565 neral.* 83 (9–10), 952–969. doi:10.2138/am-1998-9-1004.

566 Escartín, J., Mevel, C., MacLeod, C.J., McCaig, A.M., 2003. Constraints on deformation conditions
567 and the origin of oceanic detachments: The Mid-Atlantic Ridge core complex at 15°45'N
568 Constraints on deformation conditions and the origin of oceanic detachments: the Mid-Atlantic Ridge core com-
569 plex at 15°45'N. *Geochem. Geophys. Geosyst.* 4, 1067. doi:10.1029/2002GC000472.

570 Faak, K., Gillis, K., 2016. Slow cooling of the lowermost oceanic crust at the fast-spreading East
571 Pacific Rise
572 Slow cooling of the lowermost oceanic crust at the fast-spreading East Pacific rise.
Geology 44, 115–118. doi:10.1130/G37353.1.

573 Fallourd, S., Poujol, M., Boulvais, P., Paquette, J.L., de Saint Blanquat, M., Rémy, P., 2014. In situ
574 LA-ICP-MS U-Pb titanite dating of Na-Ca metasomatism in orogenic belts : the North Pyrenean
575 example. *Int. J. Earth Sci.* 103, 667–682.

576 France, L., Lombard, M., Nicollet, C., Berthod, C., Debret, B., Koepke, J., Ildefonse, B., Toussaint,
577 A., 2021. Quantifying the axial magma lens dynamics at the roof of oceanic magma reservoirs (dike
578 / gabbro transition): Oman Drilling Project GT3 site survey. *J. Geophys. Res. Solid Earth*.
579 doi:10.1029/2020JB021496.

580 Gillis, K.M., Coogan, L.A., 2019. A review of the geological constraints on the conductive bound-
581 ary layer at the base of the hydrothermal system at mid-ocean ridges. *Geochem. Geophys. Geo-*
582 *syst.* 20, 67–83. doi:10.1029/2018gc007878.

583 Gonçalves, G.O., Cristiano Lana, C., Scholz, R., Buick, I.S., Gerdes, A., Kamo, S.L., Corfu, F., Ma-
584 rinho, M.M., Chaves, A.O., Valeriano, C., Nalini Jr., H.A., 2016. An assessment of monazite from
585 the Itambé pegmatite district for use as U–Pb isotope reference material for microanalysis and impli-
586 cations for the origin of the “Moacyr” monazite. *Chemical Geology* *Chem. Geol.* 424 (30), 50.

587 Griffin, W., 2008. GLITTER: data reduction software for laser ablation ICP-MS. *Laser Ablation*
588 *ICP-MS in the Earth Sciences: Current practices and outstanding issues* GLITTER: Data Reduction
589 *Software for Laser Ablation ICP-MS. Laser Ablation ICP-MS in the Earth Sciences: Current Prac-*
590 *tices and Outstanding Issues.* pp. 308–311.

591 Harigane, et al., 2019. Melt–fluid infiltration along detachment shear zones in oceanic core com-
592 plexes: Insights from amphiboles in gabbro mylonites from the Godzilla Megamullion, Parece Vela
593 Basin, the Philippine Sea. *Lithos* 344–345, 217–231.

594 Heaman, L.M., 2009. The application of U–Pb geochronology to mafic, ultramafic and alkaline
595 rocks: an evaluation of three mineral standards. *Chem Geol/Chem. Geol.* 261, 43–52.
596 doi:10.1016/j.chemgeo.2008.10.021.

597 Hiess, J.J., Condon, D.J., McLean, N.N., Noble, S.R., 2012. $^{238}\text{U}/^{235}\text{U}$ systematics in terres-
598 trial uranium-bearing minerals. *Science* 335, 1610–1614.

599 Holland, T., Blundy, J., 1994. Non-ideal interactions in calcic amphiboles and their bearing on am-
600 phibole-plagioclase thermometry. *Contr. Mineral. and Petrol.* 116, 433–447.
601 doi:10.1007/BF00310910.

602 Hoskin, P.W.O., PD, Kiinny, Wyborn, D.D., Chappell, B.W.,
603 2000. Identifying Accessory Mineral Saturation during Differentiation in Granitoid Magmas: an In-
604 tegrated Approach. *J. Petrol.* 41, 1365–1396. doi:10.1093/petrology/41.9.1365.

605 Hurai, V.V., Paquette, J.L., Huraiová, M.M., Konečný, P.P., 2010. Age of deep crustal magmatic
606 chambers in the intra-Carpathian back-arc basin inferred from LA-ICPMS U-Th-Pb dating of zircon
607 and monazite from igneous xenoliths in alkali basalts. *J. Volcanol. Geotherm. Res.* 198, 275–287.

608 Jackson, S.E., Pearson, N.J., Griffin, W.L., Belousova, E.A., 2004. The application of
609 laser ablation-inductively coupled plasma-mass spectrometry to in situ U–Pb zircon geochronology.
610 *Chemical Geology/Chem. Geol.* 211, 47–69.

611 Jaffrey, A.H., Flynn, K.F., Glendenin, L.E., Bentley, W.C., Essling, A.M., 1971. Precision mea-
612 surement of half-lives and specific activities of ^{235}U and ^{238}U . *Phys. Rev. C* 4, 1889–1906.

613 Jochum, K.P., Willbold, M., Raczek, I., Stoll, B., Herwig, K., 2005. Chemical Characterisation of
614 the USGS Reference Glasses GSA-1G, GSC-1G, GSD-1G, GSE-1G, BCR-2G, BHVO-2G and
615 BIR-1G Using EPMA, ID-TIMS, ID-ICP-MS and LA-ICP-MS. Chemical Characterisation of the
616 USGS Reference Glasses GSA-1G, GSC-1G, GSD-1G, GSE-1G, BCR-2G, BHVO-2G and BIR-1G

616 using EPMA, ID-TIMS, ID-ICP-MS and LA-ICP-MS. *Geostandards and Geoanalytical*
617 *Research*Geostand. *Geoanal. Res.* 29, 285–302.

618 Leake, B.E., Woolley, A.R., Arps, C.E.S., Birch, W.D., Gilbert, M.C., Grice, J.D., Hawthorne, F.C.,
619 Kato, A., Kisch, H.J., Krivovichev, V.G., Linthout, K., Laird, J., Mandarino, J.A., Maresch, W.V.,
620 Nickel, E.H., Rock, N.M.S., Schumacher, J.C., Smith, D.C., Stephenson, N.C.N., Ungaretti, L.,
621 Whittaker, E.J.W., Guo, Y., 1997. Nomenclature of amphiboles: report of the subcommittee on am-
622 phiboles of the International Mineralogical Association, Commission on New Minerals and Mineral
623 Names. *Canadian Mineralogist*Can. *Mineral.* 35, 219–246.

624 Leshner, C.E., Spera, F.J., 2015. *Thermodynamic and Transport Properties of Silicate Melts and*
625 *Magma*. Academic Press, Elsevier. *The encyclopedia of volcanoes*, pp. 113–141.

626 Li, X.H., Faure, M., Lin, W., Manatschal, G., 2013. New isotopic constraints on age and magma ge-
627 nesis of an embryonic oceanic crust: The Chenaillet Ophiolite in the Western AlpsNew isotopic
628 constraints on age and magma genesis of an embryonic oceanic crust: the Chenaillet Ophiolite in
629 the Western Alps. *Lithos* 160-161, 283–291. doi:10.1016/j.lithos.2012.12.016.

630 Ludwig, K.R., 2001. *User's Manual for Isoplot/Ex Version 2.49, A Geochronological Toolkit for*
631 *Microsoft Excel*. Berkeley Geochronological Center, Special Publication 1a, Berkeley, USA 55 pp.

632 Manatschal, G., Müntener, O., 2009. A type sequence across an ancient magma-poor ocean–conti-
633 nent transition: the example of the western Alpine Tethys ophiolites. *Tectonophysics* 473, 4–19.
634 doi:10.1016/j.tecto.2008.07.021.

635 Manatschal, G., Sauter, D., Karpoff, A.M., Masini, E., Mohn, G., Lagabrielle, Y., 2011. The Che-
636 naillet Ophiolite in the French/Italian Alps: an ancient analogue for an Oceanic Core Complex?The
637 Chenaillet Ophiolite in the French/Italian Alps: an ancient analogue for an Oceanic Core complex?
638 *Lithos* 124, 169–184.

639 McCaig, A.M., Delacour, A., Fallick, A.E., Castelain, T., Früh-Green, G.L.G.L., 2010. Detachment
640 fault control on hydrothermal circulation systems: Interpreting the subsurface beneath the TAG hy-
641 drothermal field using the isotopic and geological evolution of oceanic core complexes in the Atlan-
642 tic. In: Rona, P.A.P.A. (Ed.), et al., Diversity of Hydrothermal Systems on Slow Spreading Ocean
643 Ridges. Geophysical Monograph, 188. American Geophysical Union, Washington DC, pp. 207–
644 239. doi:10.1029/2008GM000729.

645 McCarthy, A., Tugend, J., Mohn, G., 2021. Formation of the Alpine Orogen by amagmatic conver-
646 gence and assembly of previously rifted lithosphere. Formation of the Alpine Orogen by amagmatic
647 convergence and assembly of previously rifted lithosphere. *Elements* 17, 29–34. doi:10.2138/gsele-
648 ments.17.1.29.

649 Mevel, C., Caby, R., Kienast, J.-R., 1978. Amphibolite facies conditions in the oceanic crust:
650 example of amphibolitized gabbro and amphibolites from the Chenaillet ophiolite massif
651 (Hautes Alpes, France). *Earth and Planetary Science Letters* 39 (1), 98–108.
652 doi:10.1016/0012-821x(78)90146-2.

653 Molina, J.F., Cambeses, A., Moreno, J.A., Morales, I., Montero, P., Bea, F., 2021. A reassessment of
654 the amphibole-plagioclase NaSi-CaAl exchange thermometer with applications to igneous and high-
655 grade metamorphic rocks. *American Mineralogist* 106, 782–800. doi:10.2138/am-
656 2021-7400.

657 Otten, M. T.M.T., 1984. The origin of brown hornblende in Artfjallet gabbro and dolerites. *Contrib.*
658 *Mineral. Petrol.* 86, 189–199.

659 Paquette, J.L.J.L., Piro, J.L., Devidal, J.L.J.L., Bosse, V.V., Didier, A.A., 2014. Sensitivity enhance-
660 ment in LA-ICP-MS by N₂ addition to carrier gas: application to radiometric dating of U-Th-bea-
661 ring minerals. *Agil. ICP-MS J.* 58, 4–5.

- 662 Paquette, J.L., Ballèvre, M., Peucat, J.J., Cornen, G., 2017. From opening to subduction of an
663 oceanic domain constrained by LA-ICP-MS U-Pb zircon dating (Variscan belt, Southern Armorican
664 Massif, France). *Lithos* 294-295, 418–437.
- 665 Peacock, S. M.S.M., 1989. Thermal modeling of metamorphic pressure-temperature-time paths: A
666 forward approach. In: Spear, F. S.F.S., Peacock, S. M.S.M. (Eds.), *Metamorphic Pressure-Tempera-*
667 *ture-Time Paths*. AGU, Washington, D. C, pp. 57–102 Short Course in Geology, 7.
- 668 Pertsev, A.N., Aranovich, L.Y., Prokofiev, V.Y., Bortnikov, N.S., Cipriani, A., Simakin, S.S., Bori-
669 sovskiy, S.E., 2015. Signatures of residual melts, magmatic and seawater-derived fluids in oceanic
670 lower-crust gabbro from the Vema lithospheric section, Central Atlantic. *J. Petrol.* 56, 1069–1088.
671 doi:10.1093/petrology/egv028.
- 672 Prowatke, S., Klemme, S., 2005. Effect of melt composition on the partitioning of trace elements
673 between titanite and silicate melt. *Geochim Cosmochim Acta* *Geochim. Cosmochim. Acta* 69, 695–
674 709. doi:10.1016/j.gca.2004.06.037.
- 675 Putirka, K., 2016. Amphibole thermometers and barometers for igneous systems and some implica-
676 tions for eruption mechanisms of felsic magmas at arc volcanoes. *American Mineralogist* *Am. Mine-*
677 *ral.* 101 (4), 841–858.
- 678 Rampone, E., Sanfilippo, A., 2021. The heterogeneous Tethyan oceanic lithosphere of the Alpine
679 ophiolites. *Elements* 17, 23–28. doi:10.2138/gselements.17.1.23.
- 680 Spear, F.S., 1989. Petrologic determination of metamorphic pressure-temperature-time paths. In:
681 Spear, F.S., Peacock, S.M. (Eds.), *Metamorphic Pressure-Temperature-Time Paths*, Short Course in
682 *Geology*. American Geophysical Union, Washington, DC, pp. 1–55.

683 Spear, F. S.F.S., Peacock, S. M.S.M., 1990. Metamorphic P-T-t paths: Program manual and compu-
684 ter exercises for the calculation of metamorphic phase equilibria, pressure-temperature-time paths
685 and thermal evolution of orogenic belts. *Metamorphic P-T-T Paths: Program Manual and Computer*
686 *Exercises for the Calculation of Metamorphic Phase Equilibria, Pressure-Temperature-Time Paths*
687 *and Thermal Evolution of Orogenic Belts*. Geological Society of America short course, Dallas,
688 Texas, p. 188.

689 Spear, F.S., Peacock, S.M., Kohn, M.J., Florence, F.P., Menard, T., 1991. Computer programs for
690 petrologic PTt path calculations. *Amer. Mineral.* 76 (11–12), 2009–2012.

691 Tera, F., Wasserburg, G.J., 1972. U-Th-Pb systematics in three Apollo 14 basalts and the problem of
692 initial Pb in lunar rocks. *Earth Planet. Sci. Lett.* 14, 281–304.

693 Tomascak, P.B., Krogstad, E.J., Walker, R.J., 1996. U-Pb Monazite Geochronology of Granitic
694 Rocks from Maine: implications for Late Paleozoic Tectonics in the Northern Appalachians. *J.*
695 *Geol.* 104, 2.

696 Tribuzio, R., Garzetti, F., Corfu, F., Tiepolo, M., Renna, M.R., 2016. U–Pb zircon geochronology of
697 the Ligurian ophiolites (Northern Apennine, Italy): implications for continental breakup to slow
698 seafloor spreading. *Tectonophysics* 666, 220–243. doi:10.1016/j.tecto.2015.10.024.

699 Tribuzio, R., Manatschal, G., Renna, M.R., Ottolini, L., Zanetti, A., 2019. Tectono-magmatic inter-
700 play and related metasomatism in gabbros from the Chenaillet ophiolite (Western Alps). *Journal of*
701 *Petrology*. *J. Petrol.* 60, 2483–2508. doi:10.1093/petrology/egaa015.

702 van Achterbergh, E.E., Ryan, C.G., Jackson, S.E., Griffin, W.W., 2001. Data reduction soft-
703 ware for LA-ICP-MS. In: Sylvester, P.P. (Ed.), *Laser Ablation-ICPMS in the Earth Sciences*, 29. Mi-
704 *neralogical Association of Canada*, pp. 239–243.

705 Whitney, D.L., Evans, B.W., 2010. Abbreviations for names of rock-forming minerals. American
706 MineralogistAm. Mineral. 95, 185–187. doi:10.2138/am.2010.3371.

707 Wiedenbeck, MM., Allé, PP., Corfu, FF., Wl, Griffin, Meier, MM., Oberli, FF., Quadt, AVA.V., Rod-
708 dick, JCJ.C., Spiegel, WW., 1995. Three natural zircon standards for U-Th-Pb, Lu-Hf, trace element
709 and REE analyses. Geostand. Newslett. 19, 1–23.

710 Zhang, C., Koepke, J., Kirchner, C., Götze, N., Behrens, H., 2014. Rapid hydrothermal cooling
711 above the axial melt lens at fast-spreading mid-ocean ridge. Sci. Rep. 4, 6342.
712 doi:10.1038/srep06342.

713 **Legends of the figures and tables**

714 Figure 1: Geological map of the Chenaillet Ophiolite; simplified after Manatschal et al. (2011). Red
715 spot: samples CH1 and CH4; red star: sample CH3.

716 Figure 2: Gabbroic lens (Gb) of Mont Chenaillet . It is intrusive in serpentinites (serp), themselves
717 covered by pillow basalts (Bc) on the western flank of the NW ridge of the Mont Chenaillet. Sample
718 CH3 comes from the top of this lens. View from les Prés du Gondran.

719 Figure 3: Contact between an ophitic-textured gabbro and a microgabbro. The contact is sharp and
720 could represent intrusive contact, indicative of a (possible) local replenishment of the magmatic lens.

721 Figure 4: Metagabbro (CH3), a few meters from the gabbro-serpentinite contact (on the top of the
722 gabbro outcrop of the figure 2). Grey pyroxenes and black amphiboles, both magmatic, are wrapped
723 in a foliation, which is underlined by a black amphibole. Abbreviations in text and figures are from
724 Whitney & Evans (2010).

725

726 Figure 5: Coronitic amphibole in the metagabbro CH3: the porphyroblast of brown amphibole is
727 wrapped by foliation and surrounded by green-brown amphibole and ilmenite, testifying to a ductile
728 high temperature deformation and metamorphism during cooling of the gabbro. microphotography in
729 Plane Polarized Light; white bar: 1mm.

730 Figure 6: Coronitic assemblage in the metagabbro CH3: microphotography of a pressure shadow of
731 green amphibole (gHbl) – plagioclase – titanite (Ttn) +/-ilmenite (ilm, itself replaced by titanite +
732 rutile as in fig. 9) around a brown amphibole (bHbl) (Microphotography in PPL); white bar: 0,25mm.

733 Figure 7: Complex coronitic assemblage in the metagabbro CH1: From left to the right, i.e. from the
734 magmatic clinopyroxene clasts to plagioclase: the magmatic clinopyroxene clasts (CpxMag) are re-
735 crystallized into a fine granoblastic aggregate of Cpx2 wrapped with interstitial brown hornblende
736 (Hbb) (=granulite facies). Then, a single brown amphibole gradually changes to a green hornblende
737 (GHbl) (= amphibolite facies), then to an actinolite associated with chlorite and epidote.
738 (Act+Chl+Ep) (= greenschists facies). The plagioclase ("Pl") is black with a dusty aspect: it is re-
739 placed by a fine aggregate of epidote and albite (= prehnite - pumpellyite facies). Temperatures in °C
740 according to the Ti-amphibole thermometer of Ernst and Liu (1998, « revisited »). This portion of
741 rock records on only 3mm, the cooling of the gabbro through the Granulite, Amphibolite and
742 Greenschists facies. (Microphotography in PPL); white bar: 1 mm.

743 Figure 8: A string of chronometer minerals in sample CH1: a string of titanite +/- ilmenite grains is
744 located in an amphibolitic layer with a granoblastic texture. a) and b) microphotographs in PPL. In
745 white in c) and d) respectively xenotime and monazite in the string; titanite is dark gray, ilmenite is
746 light gray. Backscattered electron (BSE) images; white bar: 0.4mm in a); 0.2 mm in b).

747 Figure 9: Destabilization of ilmenite into titanite + rutile needles. Backscattered electron (BSE) im-
748 age.); sample CH1; white bar: 20µm.

749 Figure 10 – Photography of a metatroctolite: at the contact with plagioclase, olivine is replaced by a
750 coronitic aggregate, composed of an amphibole (tremolite) enclosed by a chlorite rim according to
751 the reaction $Ol + Pl + V = chlorite + tremolite$. White bar: 1 cm

752 Figure 11 : (a) : Y vs Nb in ppm, (b) Chondrite-normalized REE patterns of the titanites of the meta-
753 gabbros CH1 and CH3. Chondrite values from Boynton (1984).

754 Figure 12 - Geochronological results: Tera–Wasserburg diagram showing the zircon data of (a) the
755 gabbro CH1 and (b) the albitite vein CH4. Cathodoluminescence images of zircons. In a), note the
756 oscillatory zoning; in b), a slight alteration is localised at the fractures; the size of the analysis spot
757 (30 μm) is smaller than the size of the fracture network.

758 Figure 13 - Geochronological results: Tera–Wasserburg diagram showing the monazite, xenotime
759 and titanite data of the string of titanite +/- ilmenite of CH1 sample.

760 Figure 14 Thermal modelling: modeled evolution of temperature with time at various points inside
761 a 150m thick gabbroic lens. From top to bottom, the temperature - time profiles represent respectively
762 the thermal evolution at the center of the intrusion (75 m) and at various distances from the contact,
763 inside the intrusion. In blue: enlargement for the first 750 years,

764

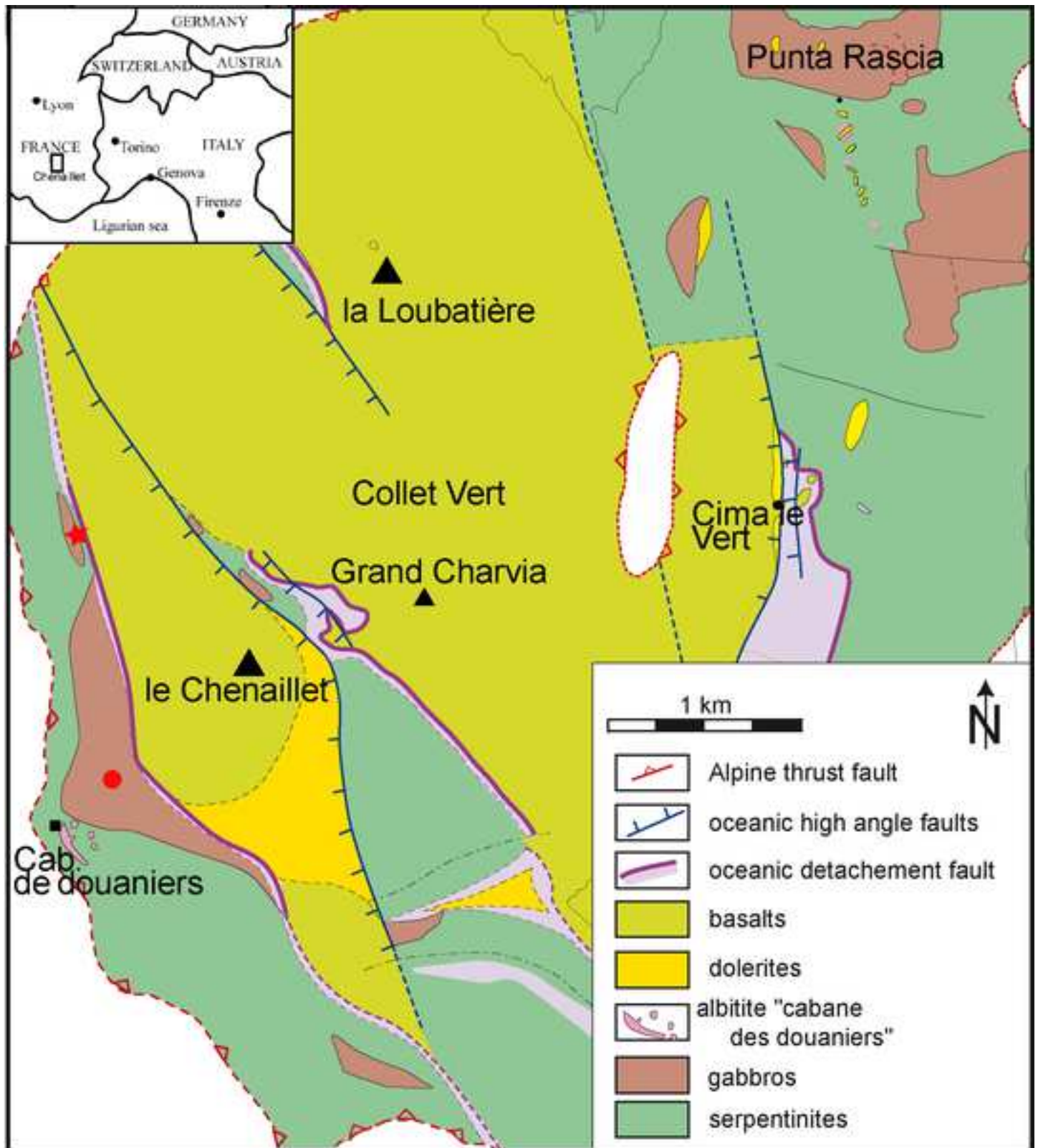
765 Table 1: Electron microprobe analyses of the major elements of amphibole – plagioclase and geother-
766 mometry; H-B : Holland and Blundy (1994), edenite-tremolite calibration. Act-String, Pl-String : ac-
767 tinolite and plagioclase of the string of titanite +/- ilmenite; Cpx: clinopyroxene; BHbl, LbHbl, GHbl:
768 brown, light brown, green hornblende; Cor : coronitic mineral. Preferred temperature estimates are
769 in bold. na: Purtika thermometer not applied on greenschist facies amphiboles.

770 Table 2: Representative analyses of titanite: major and trace elements: Electron microprobe and LA-
771 ICP-MS analyses.

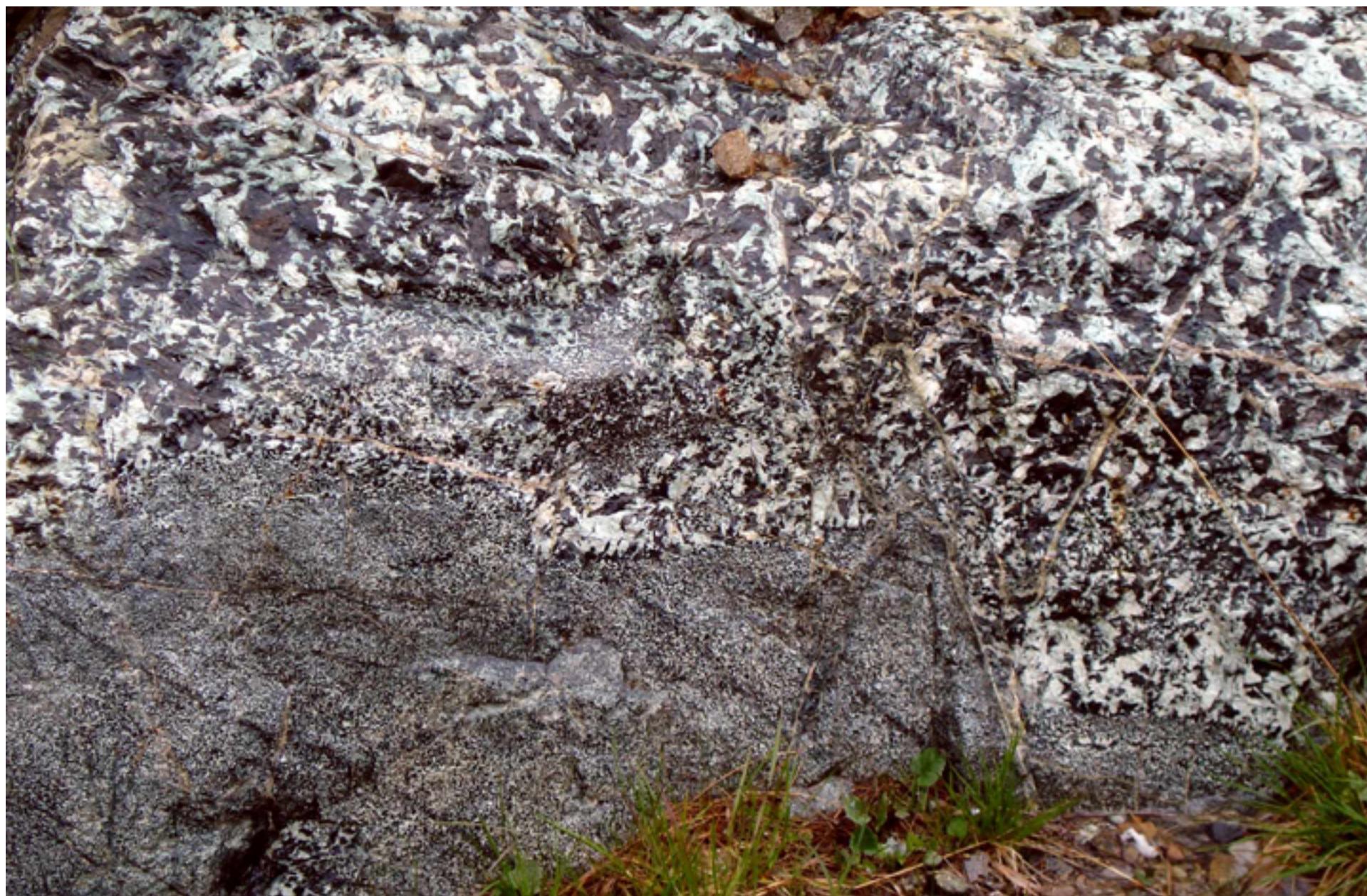
772 Table 3:U-Th-Pb dataset for the dated minerals: zircon, titanite, monazite and xenotime obtained by
773 in situ Laser Ablation ICP-MS.

774 Supplementary data 1: Mineral assemblages and main petrographic features of the studied rocks.
775 Cpx: clinopyroxene; Clast : porphyroclast; granoblastic: aggregate of Cpx₂; Cor: coronitic; Pl:
776 plagioclase, bHbl, Lb/gHbl: Brown, light brown/green hornblende; Act: actinolite; Chl: chlorite;
777 accessory minerals: titanite, ilmenite, apatite, zircon, monazite in CH1String; String: string of titanite
778 +/- ilmenite, monazite, xenotime in a tiny shear zone. +: abundant; -: rare.

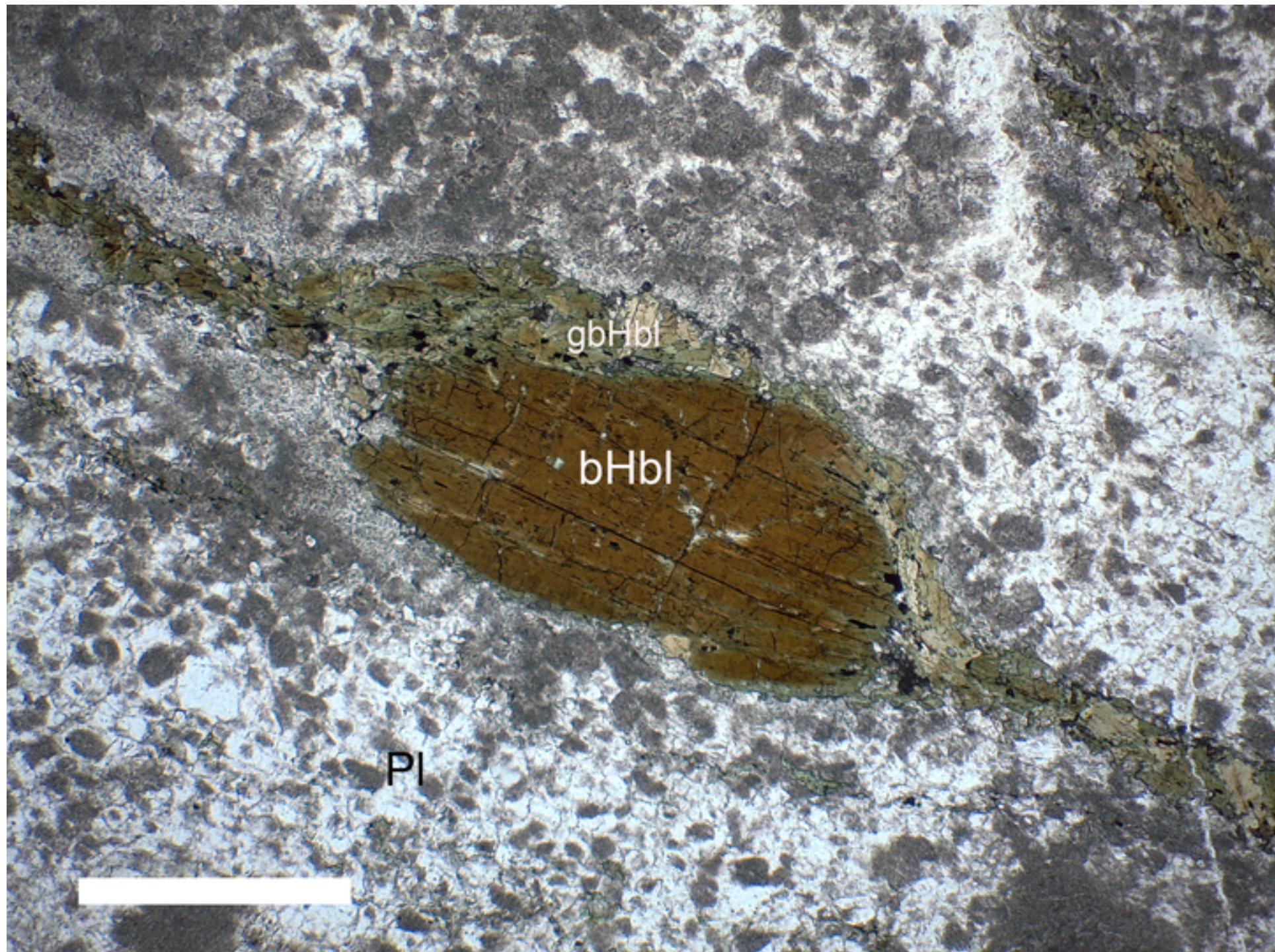
779 Supplementary data 2: Analyses of titanite: major and trace elements: Electron microprobe and LA-
780 ICP-MS analyses.

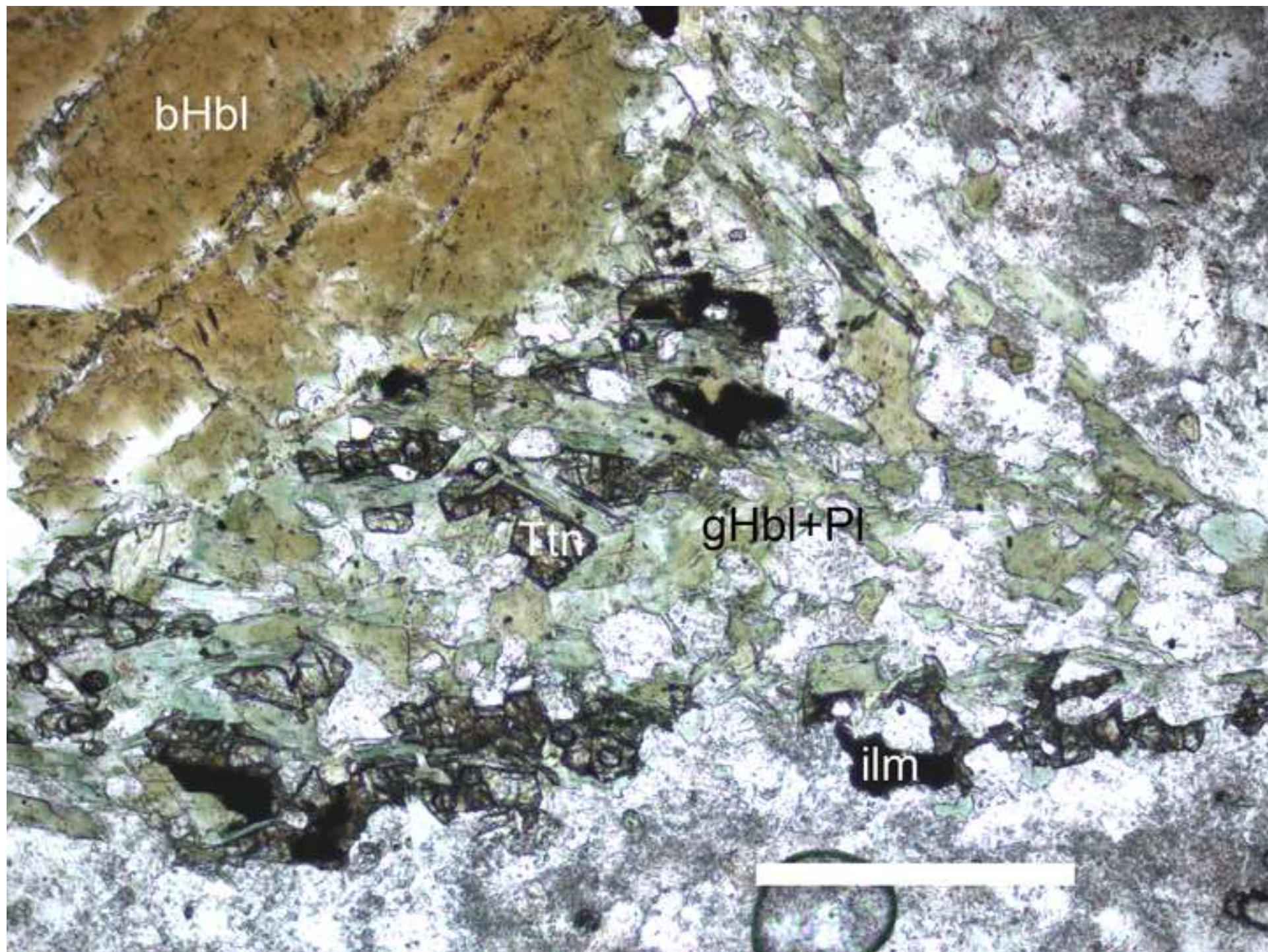


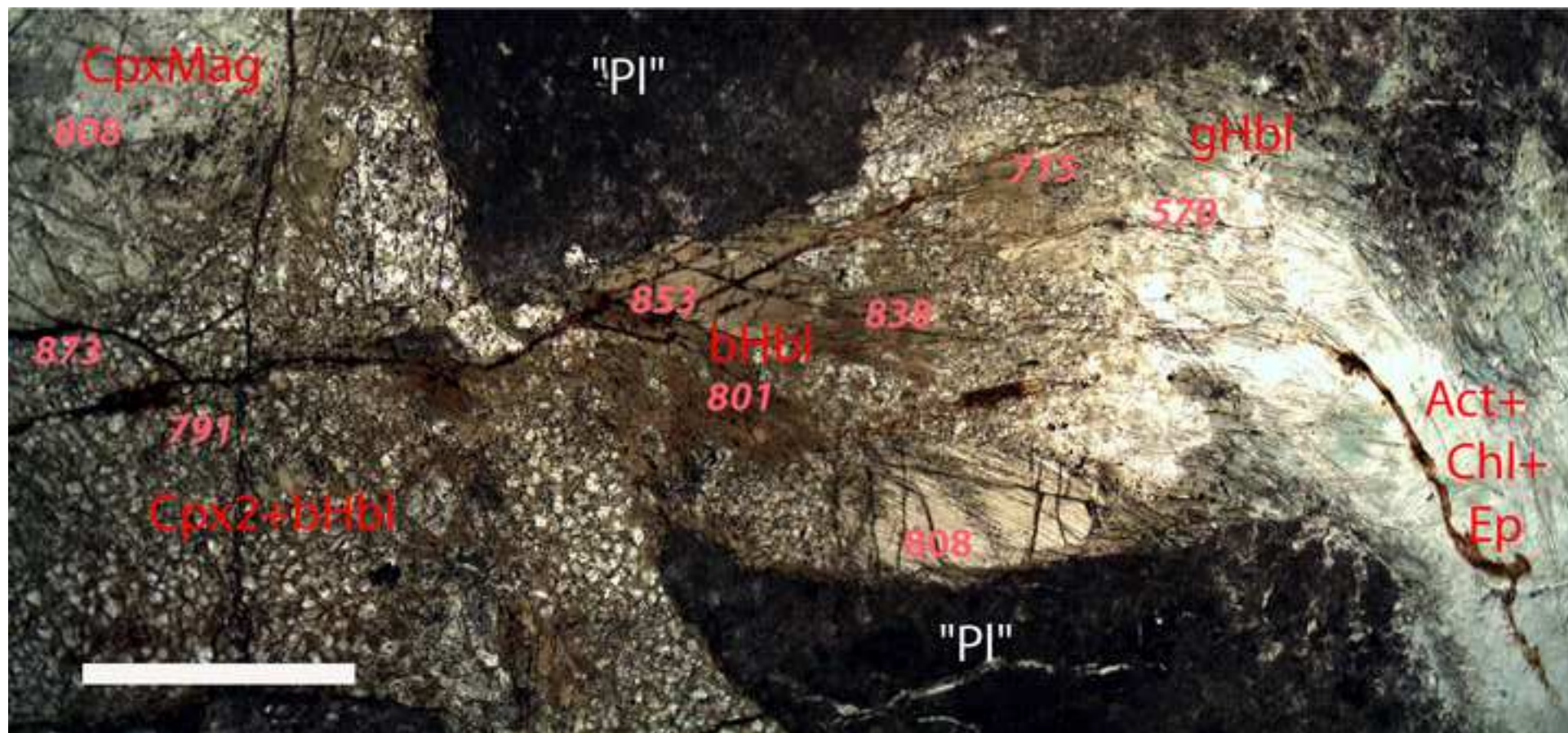


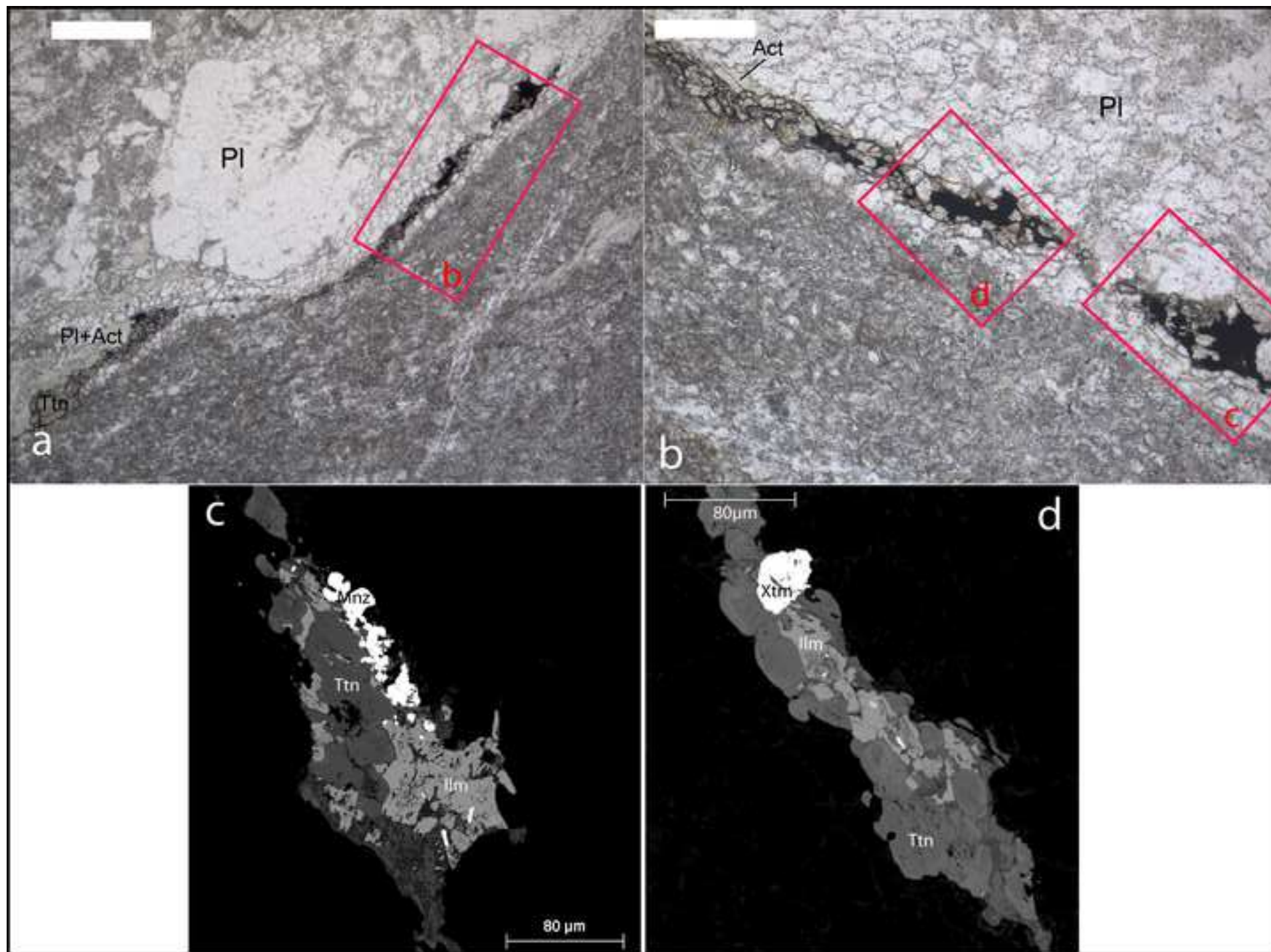


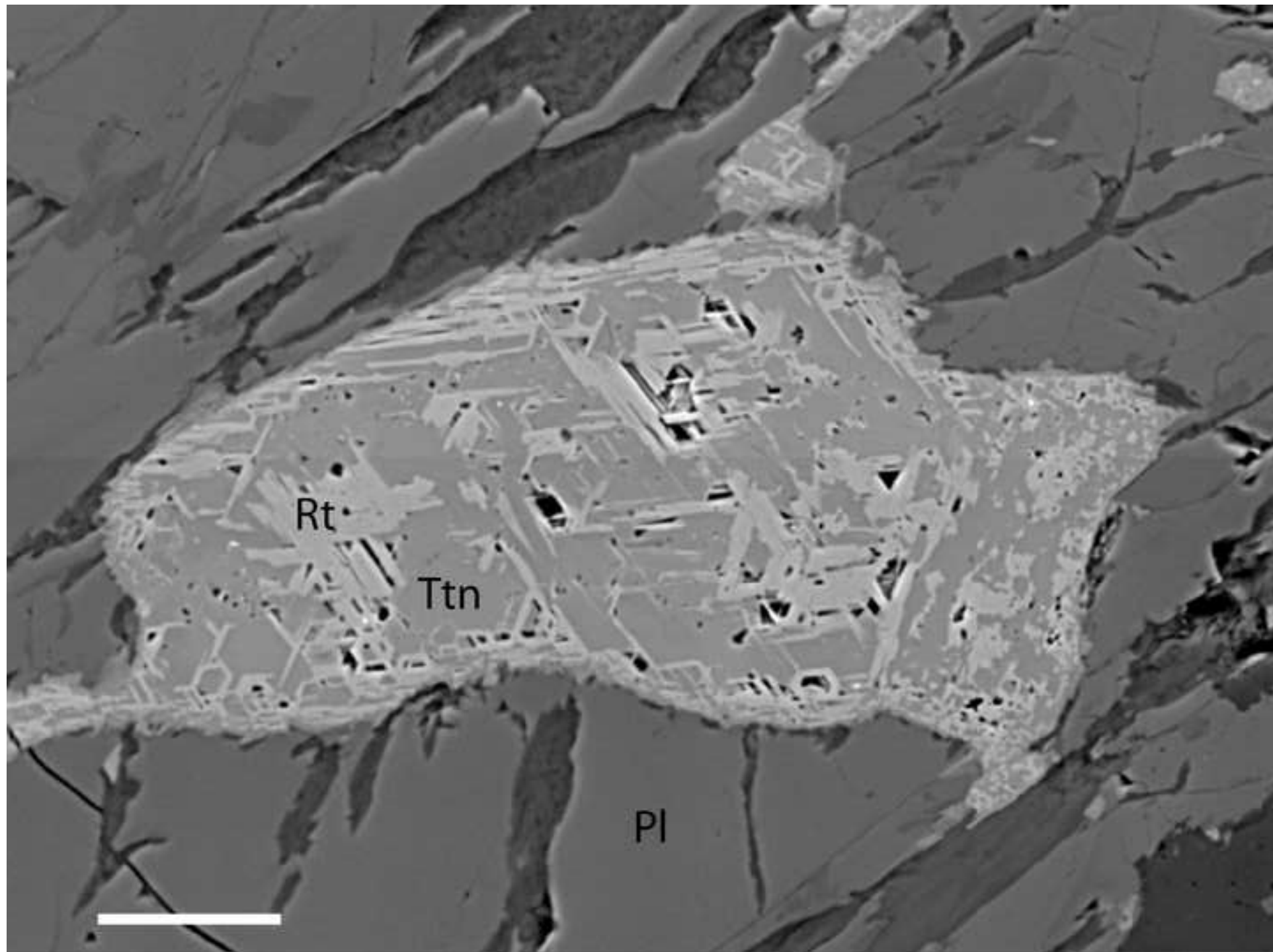


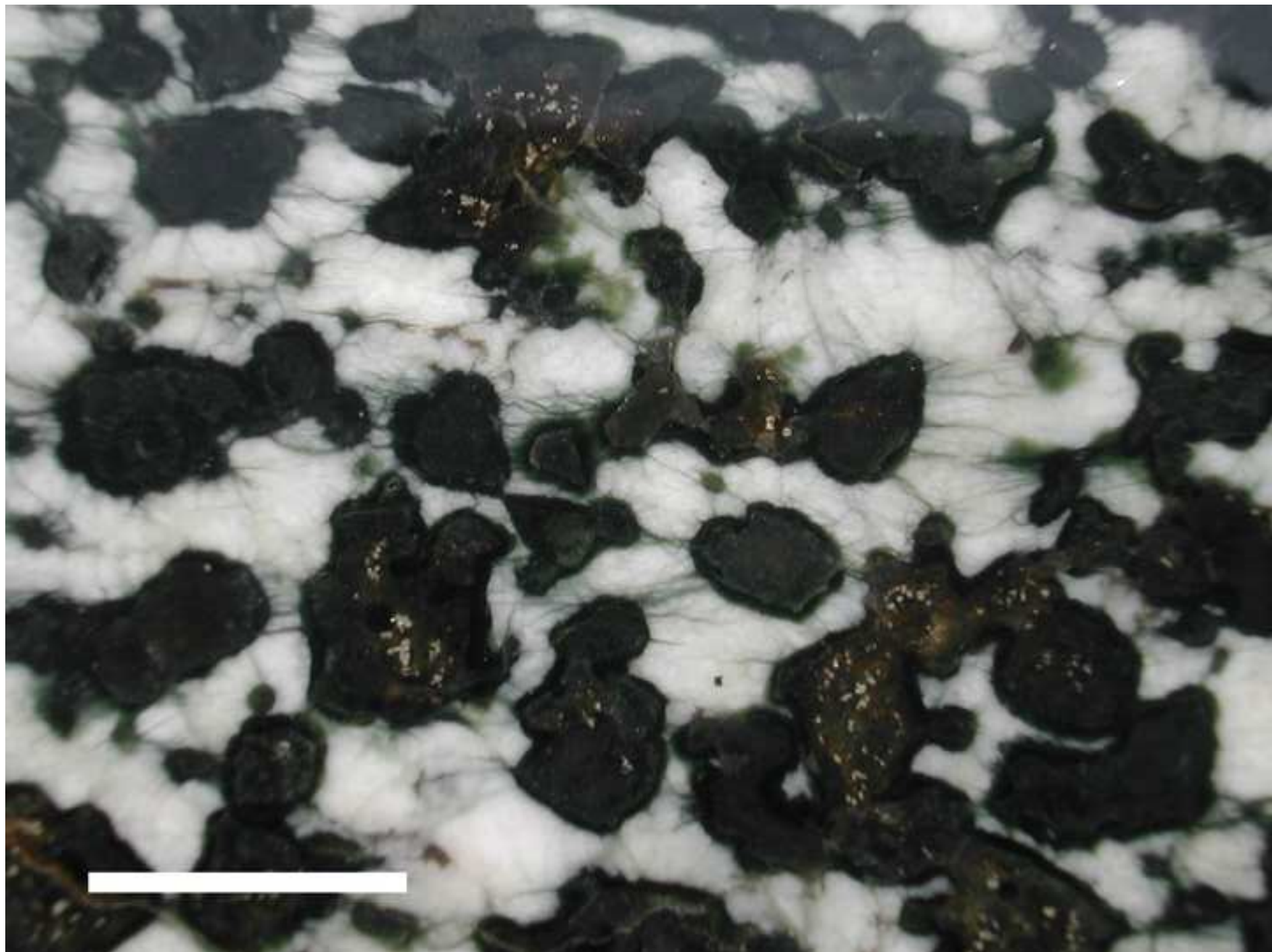




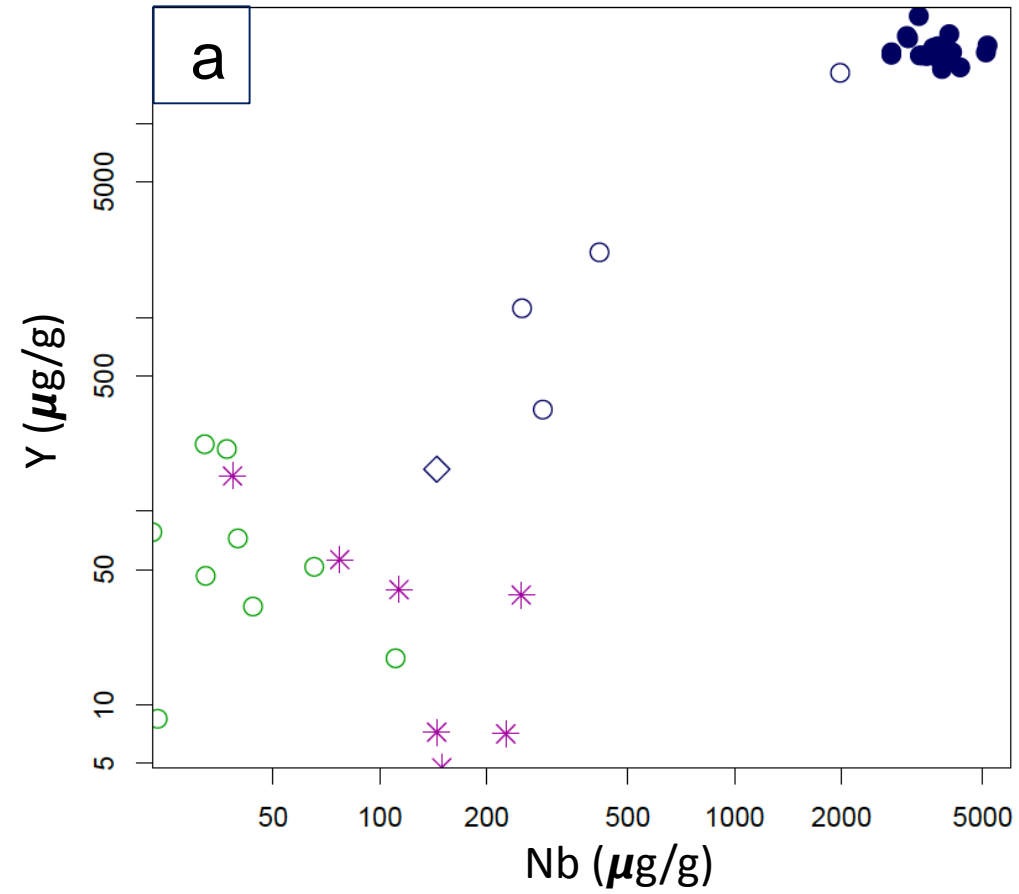


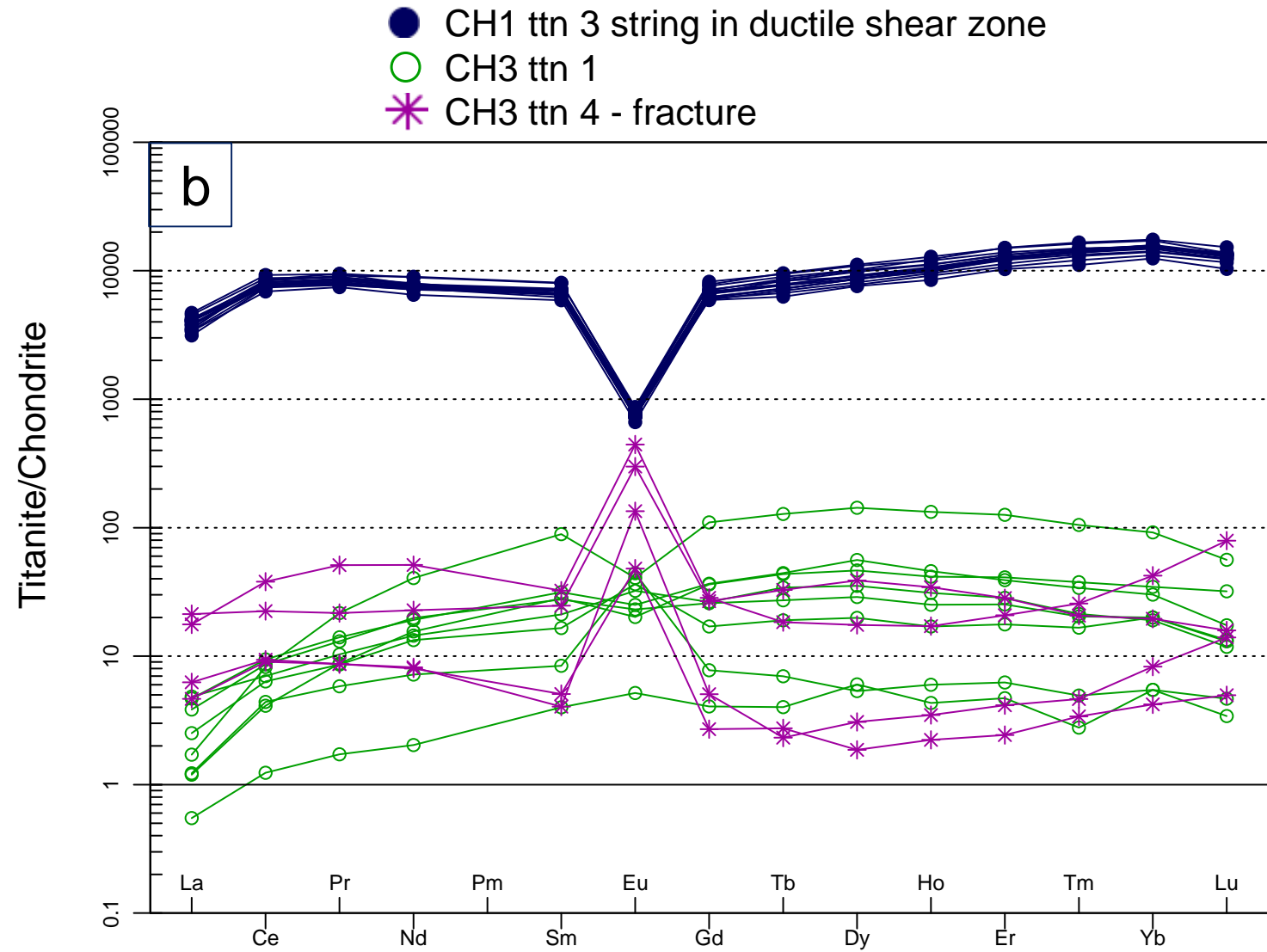


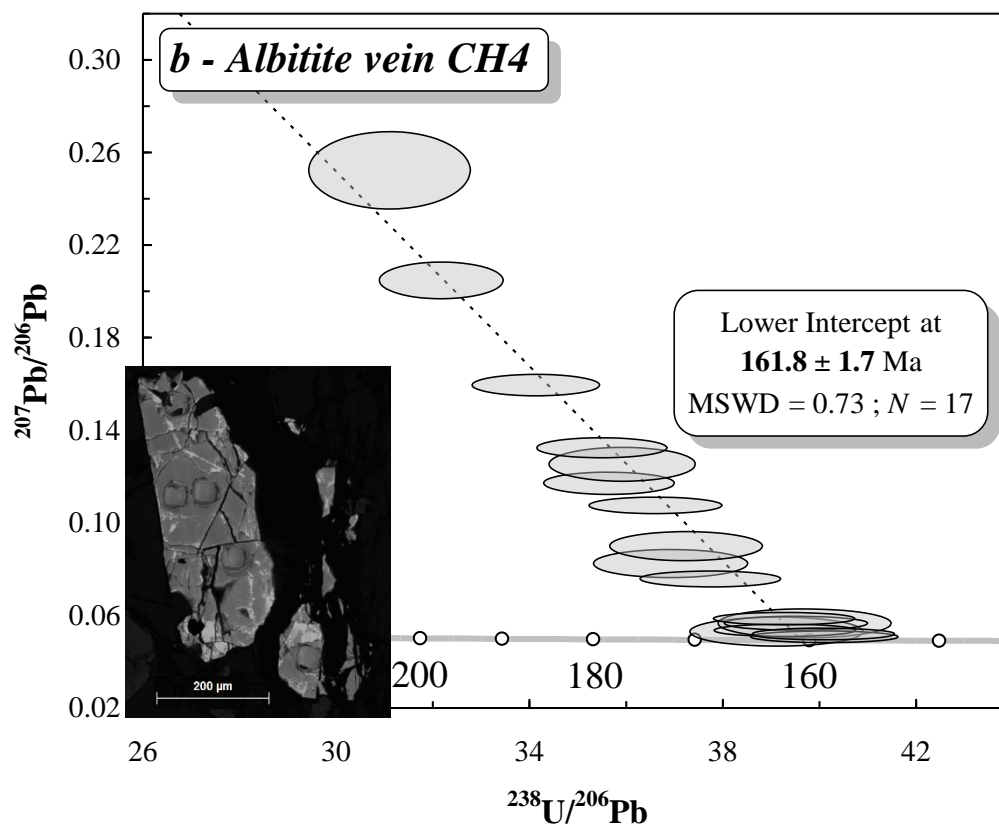
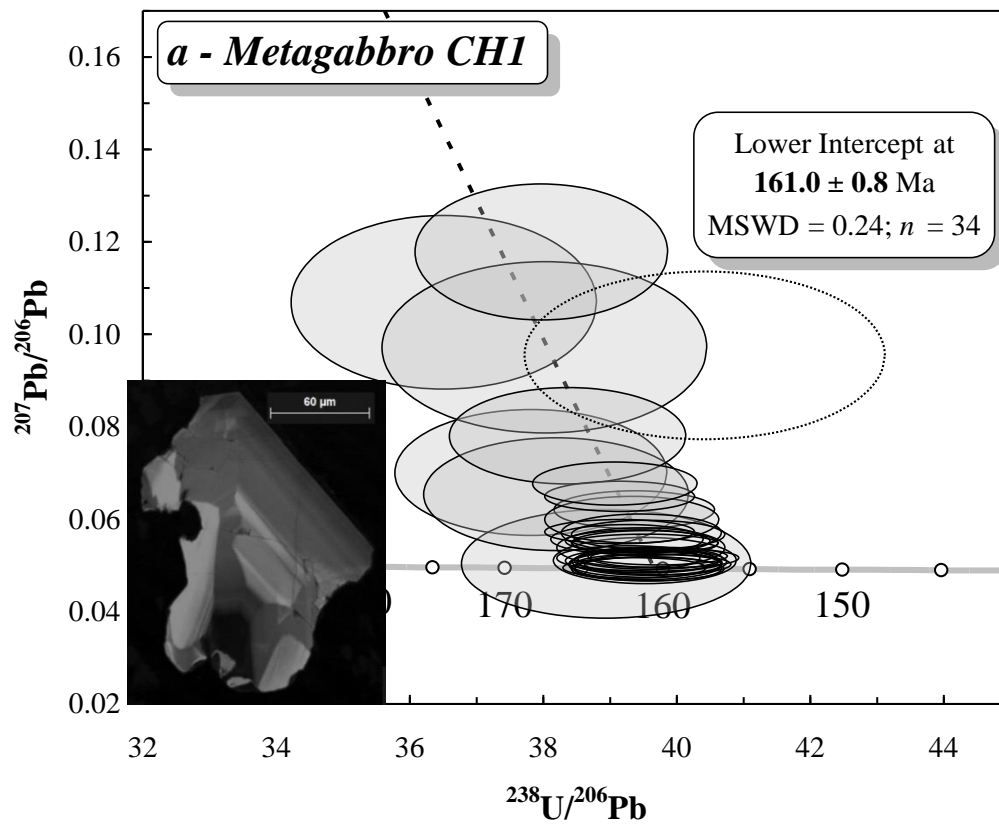


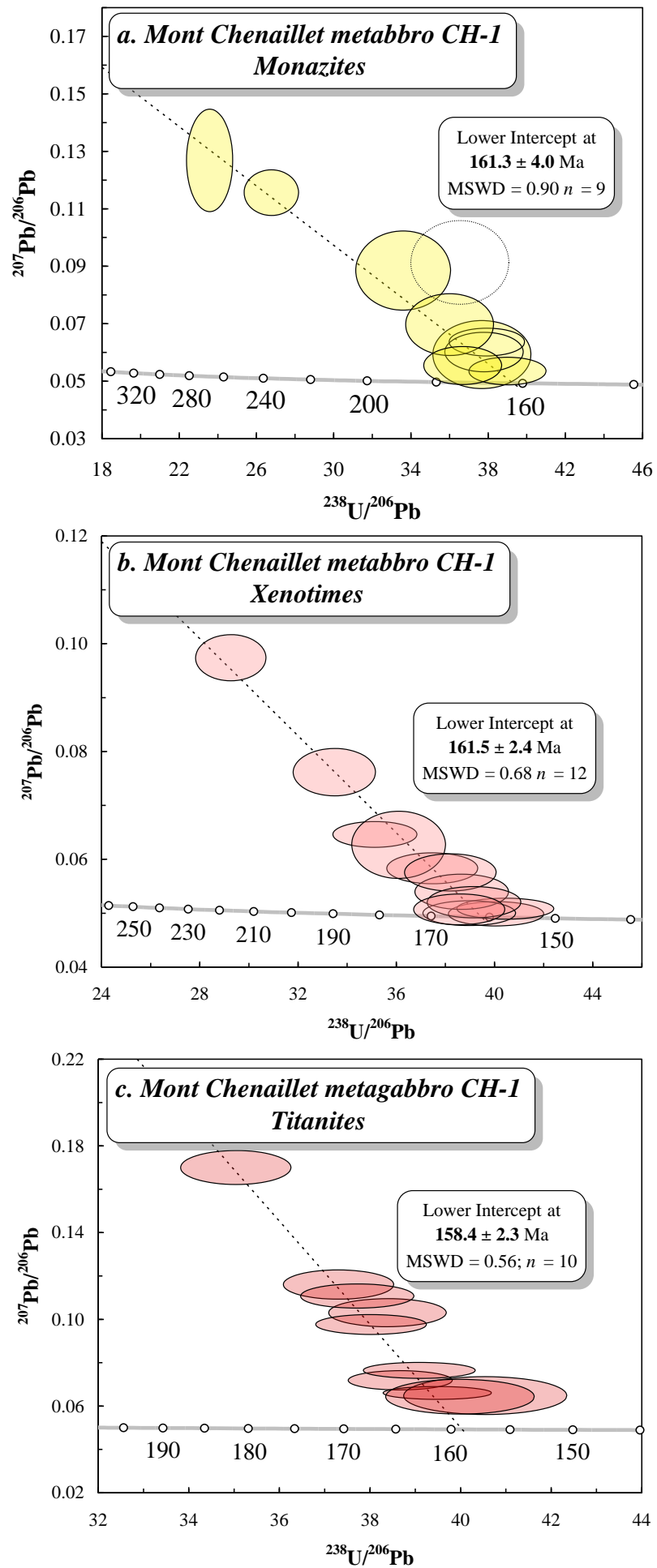


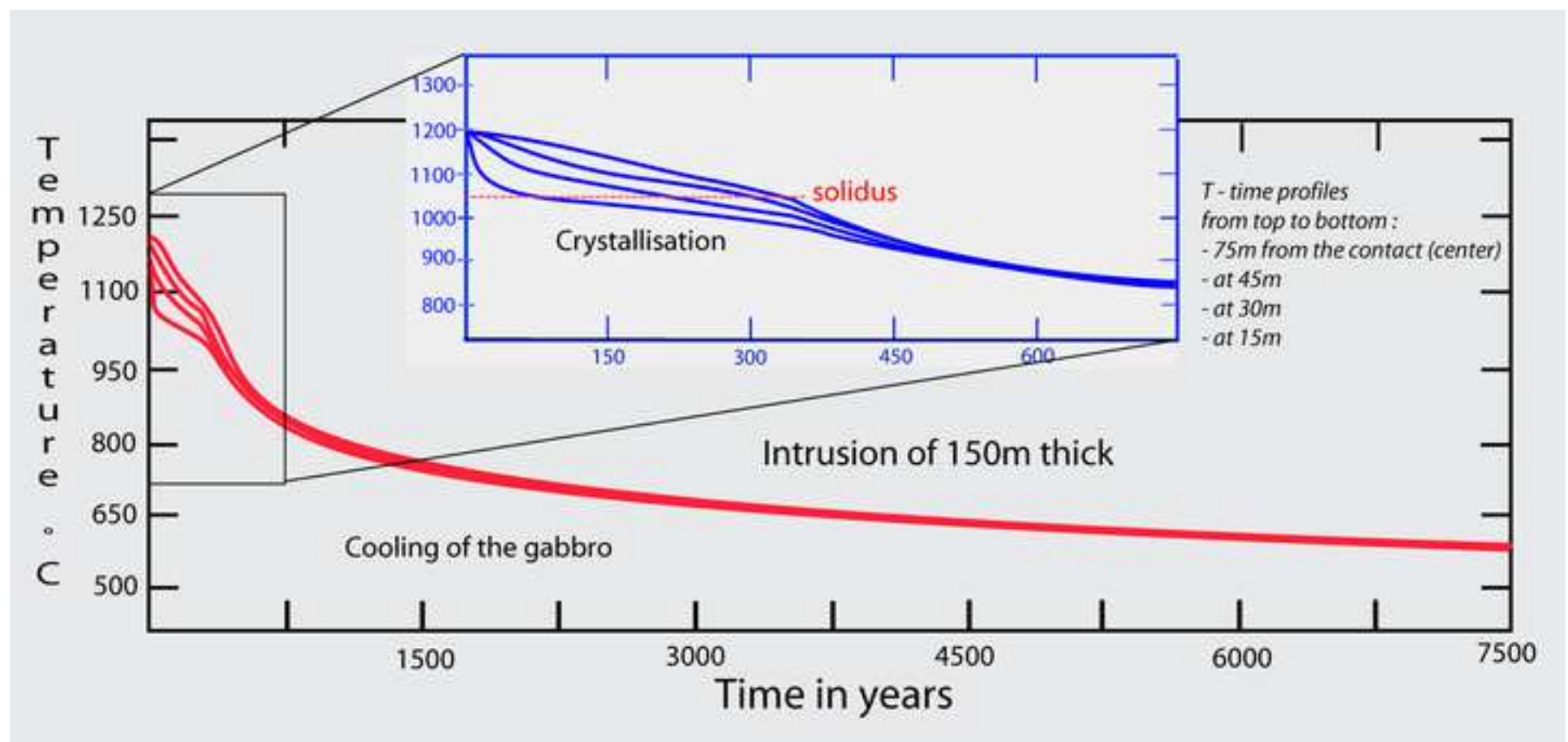
- CH1 ttn 1
- ◇ CH1 ttn 2 after ilm
- CH1 ttn 3 string in ductile shear zone
- CH3 ttn 1
- * CH3 ttn 4 in fracture











Feuille1

sample	1	2	3	4	5	6	7	8	9	10	11	12	13	14	15
	Metagabbro Ch1														
Figure	8														
mineral	Act-String	PI-String	Act-String	PI-String	Act-String	PI-String	Cpx	BHbl-Cor	BHbl-Cor	BHbl	GHbl-Cor	GHbl-Cor	BHbl-Cor	ActCor	GHblCor
SiO2	53.19	64.19	53.99	64.13	54.04	65.44	53.54	47.20	44.85	45.73	48.83	46.88	48.56	52.11	46.20
TiO2	0.57	0.00	0.50	0.00	0.41	0.03	0.21	2.25	2.66	2.62	0.46	0.39	1.90	0.08	0.36
Cr2O3		0.00		0.01		0.01	0.61				0.34	0.56			
Al2O3	3.00	22.58	2.63	22.54	2.64	21.53	1.46	7.86	8.86	9.10	6.63	10.71	7.61	3.04	7.64
FeO	9.93	0.11	9.29	0.10	8.99	0.11	3.87	10.46	11.76	11.33	11.67	10.90	8.77	17.55	20.68
MnO	0.24	0.02	0.29	0.00	0.22	0.00	0.23	0.24	0.28	0.25	0.17	0.26	0.19	0.30	0.29
MgO	17.90	0.02	18.38	0.00	18.57	0.00	15.65	14.73	13.74	15.13	15.04	14.33	16.50	12.30	8.72
CaO	11.42	3.77	11.07	3.68	11.36	2.84	23.63	11.36	11.39	10.93	12.54	12.30	12.15	12.50	11.76
Na2O	0.83	9.51	0.75	9.48	0.71	9.93	0.37	1.82	2.15	2.32	1.33	2.15	1.77	0.23	1.44
K2O	0.08	0.03	0.07	0.07	0.06	0.13	0.01	0.25	0.28	0.30	0.06	0.14	0.23	0.05	0.12
Total	97.15	100.23	96.96	100.01	97.02	100.04	99.59	96.33	96.40	97.75			97.97	98.17	97.21
Cations (Fe2+/Fe3+ charge balance)															
Si	7.488	2.829	7.557	2.833	7.567	2.885	1.970	6.890	6.637	6.557	7.086	6.702	6.934	7.610	6.983
Ti	0.060	0.000	0.053	0.000	0.043	0.001	0.006	0.247	0.296	0.282	0.050	0.042	0.204	0.009	0.041
Cr	0.000	0.000	0.000	0.000	0.000	0.000	0.018	0.000	0.000	0.000	0.039	0.063	0.000	0.000	0.000
Al	0.498	1.173	0.434	1.174	0.436	1.119	0.063	1.352	1.546	1.538	1.134	1.805	1.281	0.523	1.361
Fe3+	0.719	0.000	0.810	0.000	0.732	0.000		0.260	0.306	0.725	1.416	1.303	0.195	0.253	0.338
Fe2+	0.450	0.004	0.277	0.004	0.320	0.004	0.119	1.017	1.149	0.634	0.021	0.031	0.852	1.891	2.276
Mn	0.029	0.001	0.034	0.000	0.026	0.000	0.007	0.030	0.035	0.030	0.000	0.000	0.023	0.037	0.037
Mg	3.756	0.001	3.835	0.000	3.876	0.000	0.858	3.205	3.031	3.233	1.950	1.884	3.511	2.677	1.964
Ca	1.722	0.178	1.660	0.174	1.704	0.134	0.932	1.776	1.806	1.679	0.374	0.596	1.859	1.956	1.904
Na	0.227	0.812	0.204	0.812	0.193	0.849	0.026	0.515	0.617	0.645	0.011	0.026	0.490	0.065	0.422
K	0.014	0.002	0.012	0.004	0.011	0.007	0.000	0.047	0.053	0.055	0.000	0.000	0.042	0.009	0.023
H	2.000		2.000		2.000			2.000	2.000	2.000	0.000	0.000	2.000	2.000	2.000
Total	14.963	5.000	14.876	5.000	14.908	5.000	4.000	15.338	15.476	15.379	0.739	0.744	15.390	15.030	15.349
xMg(Fe2+)	0.89		0.93		0.92		0.88	0.76	0.73	0.84	0.74	0.74	0.80	0.59	0.46
Thermometry: T°C															
Ernst-Liu (K):1998	599		586		568			866	912	907	578	563	820	498	557
Putirka: 2016	<i>na</i>		<i>na</i>		<i>na</i>			857	890	907	783	851	860	<i>na</i>	715
H-B: 1994	596		545		548									500	650
Anorthite		0.18		0.18		0.14									
Albite		0.82		0.82		0.86									
Orthoclase		0.00		0.00		0.01									

16	17	18	19	20	21	22	23	24	25	26	27	28	29	30	31	32
Metagabbro Ch3																
6												5				
PICor	ActCor	BHbl	PI	BHbl	BHbl	LbHblCor	PICor	LbHblCor	LbHblCor	LbHblCor	LbHblCor	BHbl	BHbl	BHbl	BHbl	BHbl
68.230	51.73	44.05	65.15	44.46	44.37	45.91	66.09	47.59	45.82	46.55	46.51	44.88	44.54	44.54	44.90	44.83
0.020	0.32	2.97	0.00	2.76	3.00	1.49	0.03	1.38	1.73	1.62	1.51	3.02	3.07	2.82	2.97	3.06
0.000			0.00				0.00									
20.890	3.54	9.37	21.78	9.13	8.62	8.15	21.38	6.58	7.47	7.35	7.06	8.57	8.73	8.66	8.51	8.51
0.220	16.21	14.50	0.11	14.66	15.67	15.49	0.11	15.45	15.68	15.63	15.42	16.05	15.71	15.69	16.06	15.67
0.000	0.27	0.38	0.00	0.49	0.54	0.52	0.02	0.52	0.51	0.55	0.48	0.55	0.60	0.58	0.59	0.56
0.010	12.97	12.95	0.00	13.15	12.65	13.11	0.00	13.69	12.76	13.35	13.53	12.45	12.49	12.42	12.10	12.25
1.610	12.15	9.89	2.85	9.81	9.55	9.97	2.07	10.21	10.03	9.94	9.77	9.43	9.36	9.71	9.73	9.58
11.080	0.63	2.67	9.73	2.66	2.60	2.08	10.53	1.85	2.03	2.02	2.07	2.62	2.64	2.52	2.64	2.51
0.030	0.09	0.22	0.17	0.21	0.20	0.19	0.02	0.21	0.18	0.22	0.15	0.21	0.21	0.29	0.22	0.17
102.090	97.93	97.04	99.78	97.33	97.22	96.92	100.24	97.49	96.22	97.25	96.59	97.78	97.36	97.28	97.73	97.15
2.933	7.534	6.429	2.882	6.453	6.466	6.663	2.897	6.863	6.732	6.734	6.761	6.505	6.47679	6.50652	6.54904	6.54840
0.001	0.035	0.326	0.000	0.301	0.329	0.163	0.001	0.150	0.191	0.176	0.165	0.329	0.33568	0.30976	0.32574	0.33610
0.000	0.000	0.000	0.000	0.000	0.000	0.000	0.000	0.000	0.000	0.000	0.000	0.000	0.00000	0.00000	0.00000	0.00000
1.059	0.608	1.612	1.135	1.562	1.481	1.394	1.105	1.118	1.294	1.253	1.210	1.464	1.49637	1.49119	1.46311	1.46525
0.000	0.267	0.990	0.000	1.092	1.175	1.233	0.000	1.146	1.092	1.238	1.285	1.165	1.17915	1.06926	0.95904	1.02493
0.008	1.707	0.780	0.004	0.687	0.735	0.647	0.004	0.717	0.834	0.653	0.589	0.780	0.73110	0.84731	0.99971	0.88906
0.000	0.033	0.047	0.000	0.060	0.067	0.064	0.001	0.064	0.063	0.067	0.059	0.068	0.07390	0.07176	0.07289	0.06928
0.001	2.815	2.817	0.000	2.845	2.748	2.836	0.000	2.942	2.794	2.878	2.931	2.689	2.70701	2.70419	2.63047	2.66698
0.074	1.896	1.546	0.135	1.525	1.491	1.550	0.097	1.577	1.579	1.541	1.521	1.464	1.45817	1.51964	1.52043	1.49918
0.923	0.178	0.755	0.834	0.748	0.735	0.585	0.895	0.517	0.578	0.566	0.583	0.736	0.74423	0.71366	0.74650	0.71078
0.002	0.017	0.041	0.010	0.039	0.037	0.035	0.001	0.039	0.034	0.041	0.028	0.039	0.03895	0.05404	0.04093	0.03168
	2.000	2.000		2.000	2.000	2.000		2.000	2.000	2.000	2.000	2.000	2.00000	2.00000	2.00000	2.00000
5.000	15.090	15.343	5.000	15.313	15.263	15.171	5.000	15.133	15.191	15.148	15.133	15.239	15.24135	15.28734	15.30786	15.24164
	0.62	0.78		0.81	0.79	0.81		0.80	0.77	0.82	0.83	0.78	0.79	0.76	0.72	0.75
	549	941		922	944	761		743	796	780	764	946	950	927	941	949
	<i>na</i>	908		900	892	836		806	828	827	825	885	892	882	879	881
	565	821				758		727	750	746	742	790	794	790	787	786
0.07			0.14				0.10									
0.93			0.85				0.90									
0.00			0.01				0.00									

33	34	35
Albitite - CH4		
Hbl	Hbl	PL
46.09	47.89	67.88
1.50	1.63	0.00
		0.03
6.79	6.72	20.76
17.22	17.28	0.20
0.59	0.65	0.01
12.75	13.00	0.01
9.27	9.04	1.17
2.22	2.30	10.20
0.32	0.28	0.17
96.79	98.80	100.43
6.72291	6.81056	2.982
0.16452	0.17430	0.000
0.00000	0.00000	0.001
1.16744	1.12648	1.075
1.47315	1.46429	0.000
0.62718	0.59059	0.007
0.07289	0.07829	0.000
2.77190	2.75549	0.001
1.44861	1.37730	0.055
0.62777	0.63410	0.869
0.05954	0.05079	0.010
2.00000	2.00000	
15.13592	15.06220	5.00000
0.82	0.82	
762	782	
817	812	
735	721	
		0.06
		0.93
		0.01

Sple Micr.	CH1 sample										CH3 sample			
	ttn string			ttn from matrix			ttn in ghb corona			ttn after ilm	ttn in ghb corona		ttn from late fr:	
(wt%)	2	3	4	20	21	22	23	24	25	26	28	32	43	44
SiO2	28.63	28.88	28.60	31.61	31.09	28.99	30.77	30.79	31.23	30.72	30.99	30.73	30.91	30.74
Al2O3	1.44	1.34	1.66	4.19	2.81	1.38	1.60	1.39	3.02	0.77	1.56	2.35	1.14	1.40
F	0.12	0.01	0.07	0.28	0.08	0.05	0.09	0.10	0.13	0.12	0.04	0.15	0.09	0.12
CaO	24.61	24.81	24.50	28.03	27.98	25.47	28.38	28.42	28.58	28.36	28.65	28.73	28.63	28.96
TiO2	34.89	34.83	34.62	32.45	35.62	35.23	37.22	37.84	35.38	39.00	38.37	36.62	38.44	38.33
La2O3	0.15	0.16	0.17	0.02	bdl	0.17	0.01	bdl	bdl	bdl	bdl	bdl	bdl	0.02
Nb2O5	0.61	0.74	0.43	0.04	0.06	0.28	0.00	0.04	0.00	0.02	0.02	bdl	0.02	0.01
ZrO2	0.05	0.07	0.04	bdl	0.03	0.05	0.13	0.06	0.01	bdl	0.02	bdl	0.01	0.03
P2O5	0.06	0.08	0.04	0.01	0.00	0.06	0.01	0.03	0.01	bdl	0.07	0.10	0.03	0.01
Y2O3	3.16	2.68	3.49	0.04	0.28	2.33	0.04	0.14	0.01	0.02	0.01	bdl	bdl	0.02
FeO	1.73	1.67	1.86	1.17	0.56	1.57	0.78	0.45	0.71	0.42	0.53	0.83	0.80	0.59
MnO	0.07	0.06	0.05	0.03	0.02	0.06	0.00	0.02	0.01	bdl	bdl	0.04	0.03	0.01
Ta2O5	0.36	0.45	0.27	bdl	bdl	0.03	bdl	bdl	bdl	0.02	0.01	0.02	bdl	bdl
Cr2O3	bdl	bdl	bdl	0.00	bdl	0.46	0.05	0.16	0.02	0.01				
LA-ICPMS data (ppm)														
La	1258	1402	1048	130*		1416*	125*				0.2	0.8	1.4	5.5
Ce	6353	7088	5562								1	5.1	7.3	30.7
Pr	1041	1085	909								0.2	1.1	1.1	6.2
Nd	4537	4799	3896								1.2	8.0	4.9	30.7
Sm	1306	1270	1149								0.8	3.2	0.8	6.3
Eu	57	61	49								0.4	2.7	9.9	32.6
Gd	1709	1575	1588								1.1	4.4	1.3	7.4
Tb	364	317	343								0.2	0.9	0.1	0.9
Dy	2787	2502	2767								1.9	6.4	1.0	5.6
Ho	738	657	714								0.3	1.2	0.3	1.2
Er	2586	2248	2534								1.0	3.7	0.9	4.4
Tm	465	391	432								0.1	0.5	0.2	0.8
Yb	3291	2758	2961								1.1	4.2	1.7	8.9
Lu	428	373	402								0.1	0.4	0.5	2.6
Sc	11	9	10								bdl	bdl	1.8	2.3
V	588	553	591								247	463	594	549
Cr	608	568	986								9.1	48.8	74.1	117.3
Sr	20	20	19								15.4	30.6	39.3	47.8
Y	23416	19557	22521	335*	2170*	18328*	304*	1116*	83*	165*	8.5	32.2	7.2	36.9
Zr	571	539	449		194*	362*	998*	417*	57*		95.3	26.1	59.8	267.7
Nb	4101	4321	3326	288*	416*	1982*		252*		145*	23.7	43.9	144.6	250.3
Mo	47	54	37								0.7	5.3	3.0	2.1
Sn	274	274	220								11.7	19.4	96.3	83.4
Sb	bdl	bdl	bdl								bdl	bdl	bdl	bdl
Hf	104	91	81								2.7	1.0	2.5	9.3
Ta	3153	3405	2132			262*				120*	0.4	1.4	0.7	5.1
W	4	4	3								bdl	2.3	0.4	0.4
Pb	3	3	2								0.1	0.3	0.1	0.1
Th	176	162	136								0.0	0.0	0.1	0.6
U	163	164	154								0.0	0.1	0.5	4.6

* calculated from microprobe data

bdl = below detection limit

acture

49
30.93
2.24
0.11
28.97
36.94
bdl
bdl
bdl
0.01
bdl
0.70
0.02
bdl

6.6
18.1
2.6
13.7
4.8
21.9
6.9
1.6
12.5
2.5
5.9
0.7
4.1
0.5
7.0
363
54.5
276.2
56.2
42.6
77.1
2.8
35.1
bdl
1.9
0.8
0.1
2.4
0.1
0.6

Table 2: U-Pb data of the dated minerals from Mont Chenaillet obtained by *in situ* Laser Ablation ICP-MS

Zircon CH1 analysis	<i>Pb</i>	<i>Th</i>	<i>U</i>	Th/U	2 σ absolute			2 σ absolute error		Age (Ma)	2 σ error
	ppm ^l	ppm ^l	ppm ^l		²⁰⁷ Pb/ ²³⁵ U ²	²⁰⁷ Pb/ ²³⁵ U	²⁰⁶ Pb/ ²³⁸ U ²	²⁰⁶ Pb/ ²³⁸ U	correlation		
Zr1/#1	0.4	4.5	12	0.37	0.4028	0.0621	0.02742	0.00141	0.33	174.4	8.9
Zr1/#2	0.3	3.1	10	0.32	0.2533	0.0424	0.02648	0.00117	0.26	168.5	7.4
Zr1/#3	0.3	3.6	12	0.31	0.1757	0.0352	0.02570	0.00117	0.23	163.6	7.4
Zr1/#4	0.3	3.2	9	0.33	0.3510	0.0584	0.02633	0.00138	0.31	167.5	8.7
Zr1/#5	0.3	2.7	10	0.28	0.2336	0.0377	0.02621	0.00111	0.26	166.8	7.1
Zr2/#1	0.6	7.9	19	0.42	0.2786	0.0326	0.02609	0.00099	0.32	166.0	6.1
Zr2/#3	0.3	3.5	11	0.31	0.3246	0.0540	0.02474	0.00135	0.33	157.5	8.5
Zr5/#1	2.4	21	90	0.23	0.2148	0.0130	0.02543	0.00063	0.41	161.9	4.1
Zr5/#2	4.4	65	162	0.40	0.1686	0.0085	0.02530	0.00060	0.47	161.1	3.7
Zr5/#3	2.4	26	94	0.28	0.1752	0.0152	0.02533	0.00072	0.33	161.3	4.5
Zr5/#4	3.1	41	114	0.36	0.2075	0.0156	0.02545	0.00069	0.36	162.0	4.4
Zr4/#1	4.3	56	163	0.35	0.1756	0.0085	0.02536	0.00060	0.49	161.4	3.7
Zr4/#2	3.1	39	114	0.34	0.1927	0.0102	0.02550	0.00060	0.44	162.3	3.8
Zr4/#3	4.2	63	156	0.40	0.1684	0.0084	0.02529	0.00057	0.45	161.0	3.7
Zr4/#4	6.4	106	233	0.45	0.1714	0.0074	0.02520	0.00057	0.52	160.4	3.6
Zr4/#5	4.7	61	171	0.36	0.1992	0.0089	0.02557	0.00060	0.52	162.8	3.7
Zr4/#6	3.4	43	124	0.35	0.2266	0.0108	0.02557	0.00060	0.49	162.8	3.8
Zr4/#7	8.5	69	342	0.20	0.1740	0.0093	0.02528	0.00060	0.44	160.9	3.8
Zr3/#1	3.2	35	124	0.28	0.1946	0.0101	0.02529	0.00060	0.46	161.0	3.8
Zr3/#2	2.2	17	85	0.20	0.1852	0.0131	0.02536	0.00066	0.37	161.5	4.1
Zr3/#4	4.4	20	181	0.11	0.1719	0.0098	0.02532	0.00060	0.41	161.2	3.8
Zr6/#1	18	75	760	0.10	0.1734	0.0067	0.02528	0.00057	0.59	160.9	3.5
Zr6/#2	5.0	71	188	0.38	0.1750	0.0084	0.02531	0.00057	0.47	161.1	3.7
Zr6/#3	5.5	76	205	0.37	0.1704	0.0076	0.02543	0.00057	0.50	161.9	3.6
Zr6/#4	5.2	72	192	0.38	0.1727	0.0092	0.02533	0.00060	0.45	161.2	3.7
Zr6/#5	4.3	59	160	0.37	0.1782	0.0086	0.02549	0.00057	0.46	162.3	3.7
Zr6/#6	6.0	95	219	0.43	0.1767	0.0081	0.02528	0.00057	0.49	160.9	3.6
Zr6/#7	7.5	130	266	0.49	0.1887	0.0088	0.02533	0.00057	0.48	161.3	3.6
Zr6/#8	7.6	47	318	0.15	0.1777	0.0068	0.02520	0.00054	0.56	160.5	3.5
Zr9/#1	15	71	639	0.11	0.1759	0.0073	0.02514	0.00057	0.55	160.1	3.5
Zr9/#2	6.9	48	276	0.18	0.1882	0.0072	0.02532	0.00057	0.59	161.2	3.5

Zr9/#3	6.2	41	247	0.17	0.1904	0.0083	0.02539	0.00057	0.52	161.7	3.6
Zr7/#1	3.0	18	118	0.15	0.1965	0.0129	0.02536	0.00063	0.38	161.4	4.0
Zr7/#2	1.8	12	66	0.19	0.2367	0.0151	0.02562	0.00066	0.40	163.1	4.2
Zr8/#1	0.3	3.0	10	0.31	0.4271	0.0476	0.02636	0.00108	0.37	167.7	6.9

Zircon CH4	Pb	Th	U		2 σ absolute			2 σ absolute	error	Age (Ma)	2 σ error
analysis	ppm^l	ppm^l	ppm^l	Th/U	²⁰⁷Pb/²³⁵U²	²⁰⁷Pb/²³⁵U	²⁰⁶Pb/²³⁸U²	²⁰⁶Pb/²³⁸U	correlation	²⁰⁶Pb/²³⁸U	²⁰⁶Pb/²³⁸U
Zr1#1	0.6	2.8	7.8	0.36	1.1184	0.0779	0.03220	0.00141	0.63	204.3	8.8
Zr1#2	0.5	6.7	14.0	0.48	0.3019	0.0218	0.02712	0.00096	0.49	172.5	6.0
Zr1#3	0.4	5.6	11.2	0.50	0.3270	0.0223	0.02688	0.00093	0.51	171.0	5.9
Zr1#4	0.3	4.1	8.3	0.50	0.1803	0.0197	0.02559	0.00096	0.34	162.9	6.1
Zr1#5	0.3	4.4	8.7	0.51	0.1901	0.0194	0.02522	0.00093	0.36	160.6	5.9
Zr1#6	0.9	16.6	35.2	0.47	0.1682	0.0087	0.02496	0.00078	0.60	158.9	4.8
Zr1#7	1.4	19.5	32.5	0.60	0.6409	0.0255	0.02934	0.00093	0.80	186.4	5.7
Zr1#8	0.8	10.8	26.1	0.41	0.2707	0.0132	0.02652	0.00084	0.65	168.7	5.2
Zr1#9	0.8	14.3	30.3	0.47	0.1912	0.0104	0.02533	0.00078	0.57	161.3	5.0
Zr1#10	1.0	19.0	29.0	0.65	0.3997	0.0165	0.02735	0.00084	0.74	173.9	5.3
Zr1#11	0.7	7.4	21.2	0.35	0.4478	0.0203	0.02808	0.00087	0.68	178.5	5.6
Zr1#12	0.7	10.6	25.5	0.42	0.1816	0.0095	0.02548	0.00078	0.58	162.2	4.9
Zr1#13	0.4	4.5	11.9	0.38	0.4760	0.0285	0.02788	0.00096	0.58	177.3	6.0
Zr1#14	1.0	16.2	25.7	0.63	0.5098	0.0209	0.02820	0.00087	0.75	179.2	5.4
Zr1#15	0.8	17.4	28.6	0.61	0.1723	0.0090	0.02497	0.00075	0.58	159.0	4.8
Zr1#16	0.9	17.4	31.0	0.56	0.1995	0.0097	0.02549	0.00078	0.63	162.3	4.9
Zr1#17	0.8	10.4	17.7	0.59	0.8760	0.0402	0.03113	0.00102	0.71	197.6	6.4

Monazite CH1	Pb	Th	U		2 σ absolute			2 σ absolute	error	Age (Ma)	2 σ error
analysis	ppm^l	ppm^l	ppm^l	Th/U	²⁰⁷Pb/²³⁵U²	²⁰⁷Pb/²³⁵U	²⁰⁶Pb/²³⁸U²	²⁰⁶Pb/²³⁸U	correlation	²⁰⁶Pb/²³⁸U	²⁰⁶Pb/²³⁸U
Mz1	404	25551	1174	21.8	0.2130	0.0377	0.02658	0.00147	0.31	169.1	9.2
Mz2	622	37995	1684	22.6	0.2274	0.0173	0.02641	0.00111	0.55	168.0	6.9
Mz3	670	39293	1963	20.0	0.1849	0.0161	0.02569	0.00108	0.48	163.5	6.8
Mz4	293	17609	879	20.0	0.2158	0.0229	0.02651	0.00117	0.42	168.7	7.4
Mz5	236	9971	941	10.6	0.5941	0.0425	0.03747	0.00162	0.60	237.2	10.0
Mz6	69	2422	150	16.2	0.7410	0.0921	0.04255	0.00178	0.34	268.6	33.1
Mz7	111	5668	361	15.7	0.3603	0.0517	0.02983	0.00178	0.42	189.5	38.6
Mz8	267	15412	616	25.0	0.2629	0.0366	0.02782	0.00144	0.37	176.9	29.5

Mz9	487	29963	1192	25.1	0.2043	0.0228	0.02731	0.00123	0.40	173.7	19.2
Mz10	145	9116	517	17.6	0.3414	0.0494	0.02739	0.00156	0.39	174.2	37.4

Xenotime CH1 analysis	<i>Pb</i>	<i>Th</i>	<i>U</i>	Th/U	2 σ absolute			2 σ absolute error		Age (Ma)	2 σ error
	ppm ¹	ppm ¹	ppm ¹		²⁰⁷ Pb/ ²³⁵ U ²	²⁰⁷ Pb/ ²³⁵ U	²⁰⁶ Pb/ ²³⁸ U ²	²⁰⁶ Pb/ ²³⁸ U	correlation		
Xe1	350	662	6294	0.11	0.1702	0.0093	0.02499	0.00099	0.72	159.1	6.2
Xe2	467	1243	8366	0.15	0.1717	0.0088	0.02475	0.00099	0.78	157.6	6.2
Xe3	459	1438	6702	0.21	0.2525	0.0128	0.02851	0.00114	0.79	181.2	7.1
Xe4	414	1066	6692	0.16	0.2133	0.0123	0.02672	0.00108	0.70	170.0	6.7
Xe5	293	1086	4878	0.22	0.1910	0.0123	0.02589	0.00105	0.63	164.7	6.6
Xe6	184	525	2790	0.19	0.2382	0.0221	0.02774	0.00120	0.47	176.4	7.6
Xe7	636	853	8927	0.10	0.3129	0.0197	0.02992	0.00123	0.65	190.1	7.7
Xe8	736	6188	7910	0.78	0.4592	0.0249	0.03425	0.00138	0.74	217.1	8.6
Xe9	400	768	7232	0.11	0.1754	0.0097	0.02569	0.00102	0.72	163.5	8.3
Xe10	281	748	4780	0.16	0.2064	0.0132	0.02621	0.00105	0.63	166.8	11.1
Xe11	315	1065	5574	0.19	0.1816	0.0111	0.02556	0.00102	0.65	162.7	9.5
Xe12	375	1171	6573	0.18	0.1797	0.0110	0.02596	0.00102	0.64	165.2	9.5

Titanite CH1 analysis	<i>Pb</i>	<i>Th</i>	<i>U</i>	Th/U	2 σ absolute			2 σ absolute error		Age (Ma)	2 σ error
	ppm ¹	ppm ¹	ppm ¹		²⁰⁷ Pb/ ²³⁵ U ²	²⁰⁷ Pb/ ²³⁵ U	²⁰⁶ Pb/ ²³⁸ U ²	²⁰⁶ Pb/ ²³⁸ U	correlation		
Ti1	2.4	90	53	1.68	0.4269	0.0236	0.02683	0.00072	0.49	170.7	4.6
Ti2	2.2	78	53	1.47	0.3675	0.0215	0.02607	0.00072	0.47	165.9	4.4
Ti3	2.9	63	91	0.69	0.2526	0.0145	0.02588	0.00063	0.43	164.7	4.1
Ti4	4.0	123	127	0.96	0.2271	0.0103	0.02534	0.00063	0.55	161.3	3.9
Ti5	2.5	64	70	0.91	0.4026	0.0200	0.02653	0.00072	0.55	168.8	4.5
Ti6	4.3	115	140	0.82	0.2664	0.0128	0.02560	0.00066	0.54	162.9	4.1
Ti7	4.4	72	109	0.66	0.6684	0.0317	0.02857	0.00081	0.60	181.6	5.0
Ti8	4.0	108	115	0.94	0.3511	0.0166	0.02632	0.00069	0.56	167.5	4.3
Ti9	1.0	39	32	1.19	0.2169	0.0257	0.02468	0.00090	0.31	157.2	5.6
Ti10	0.9	48	24	2.02	0.2182	0.0239	0.02502	0.00084	0.31	159.3	5.3

1: concentration uncertainty c.20%

2: data not corrected for common-Pb

Decay constants of Jaffrey et al. (1971) used